Surface Ocean pCO_2 Seasonality and Sea-Air CO_2 Flux Estimates for the North American East Coast

Sergio R. Signorini, NASA Goddard Space Flight Center, Greenbelt, Maryland, USA, sergio.signorini@nasa.gov

Antonio Mannino, NASA Goddard Space Flight Center, Greenbelt, Maryland, USA, antonio.mannino@nasa.gov

Raymond G. Najjar, Jr., Penn State University, Dept. of Meteorology, College of Earth and Marine Sciences, University Park, Pennsylvania, USA, rgn1@psu.edu

Marjorie A. M. Friedrichs, Virginia Institute of Marine Science, College of William & Mary, Gloucester Point, Virginia, USA, marjy@vims.edu

Wei-Jun Cai, University of Delaware, School of Marine Science and Policy, Newark, Delaware, USA, wcai@udel.edu

Joe Salisbury, University of New Hampshire, Durham, New Hampshire, USA, joe.salisbury@unh.edu

Zhaohui Aleck Wang, Woods Hole Oceanographic Institute, Woods Hole, Massachusetts, USA, zawang@whoi.edu

Helmuth Thomas, Dalhousie University, Nova Scotia, Canada, helmuth@phys.ocean.dal.ca

Elizabeth Shadwick, Antarctic Climate & Ecosystems Cooperative Research Centre, University of Tasmania, Hobart, Tasmania, Australia, elizabeth.shadwick@csiro.au

Corresponding author: S. R. Signorini, NASA Goddard Space Flight Center, Code 614.8, Bldg28/RmW168, 8800 Greenbelt Rd., Greenbelt, MD 20771, USA (sergio.signorini@nasa.gov, also srsigno45@gmail.com)

Key Points

- Development of regional satellite-based pCO_2 algorithms for the North American east coast continental shelf
- Assessment of the seasonal and interannual variability of surface ocean pCO_2 and sea-air CO_2 fluxes
- Interannual estimates of the sea-air CO_2 flux show that the North American east coast continental shelf is a sink of atmospheric CO_2 ranging between 3.4 and 5.4 Tg C yr^{-1}.

Abstract

Underway and *in situ* observations of surface ocean pCO_2, combined with satellite data, were used to develop pCO_2 regional algorithms to analyze the seasonal and interannual variability of surface ocean pCO_2 and sea-air CO_2 flux for five physically and biologically distinct regions of the eastern North American continental shelf: the South Atlantic Bight (SAB), the Mid-Atlantic Bight (MAB), the Gulf of Maine (GoM), Nantucket Shoals and Georges Bank (NS+GB), and the Scotian Shelf (SS). Temperature and dissolved inorganic carbon variability are the most influential factors driving the seasonality of pCO_2. Estimates of the sea-air CO_2 flux were derived from the available pCO_2 data, as well as from the pCO_2 reconstructed by the algorithm. Two different gas exchange parameterizations were used. The SS, GB+NS, MAB, and SAB regions are net sinks of atmospheric CO_2 while the GoM is a weak source. The estimates vary depending on the use of surface ocean pCO_2 from the data or algorithm, as well as with the use of the two different gas exchange parameterizations. Most of the regional estimates are in general agreement with previous studies when the range of uncertainty and interannual variability are taken into account. According to the algorithm, the average annual uptake of atmospheric CO_2 by eastern North American continental shelf waters is found to be between 3.4 and 5.4 Tg C yr^{-1} (areal average of 0.7 to 1.0 mol CO_2 m^{-2} yr^{-1}) over the period 2003-2010.

67 **Index Terms**

68

69 4805 Biogeochemical cycles, processes, and modeling

70 4855 Phytoplankton

71 4806 Carbon Cycling

72 4820 Gases

73 0480 Remote Sensing

1.0 Introduction

Coastal oceans, despite covering a small fraction of the earth's surface, are important in the global carbon cycle because rates of carbon fixation, remineralization, and burial are much higher than the global average. A crucial difference between the coastal ocean and the open ocean is the proximity of sediments to the sea surface, providing a close coupling in space and time of the pelagic and benthic environments. Thus the shallow water column in coastal regions constitutes a close link between surface sediments and the atmosphere allowing relatively direct interactions between both the sedimentary and atmospheric compartments [*Borges et al.*, 2005; *Thomas and Borges*, 2012; *Thomas et al.*, 2009; *Thomas*, 2004]. An additional characteristic of the coastal seas and continental shelves is the high temporal and spatial variability of CO_2 fluxes [*Borges et al.*, 2005; *Borges et al.*, 2008; *Cai et al.* , 2006; *Frankignoulle and Borges*, 2001; *Shadwick et al.*, 2010; *Shadwick et al.*, 2011]. The driving factors often vary within the system at seasonal time scales, and the deduction of general patterns remains difficult, typically requiring detailed case studies.

The work of *Borges* [2005] was the first to compile a global coastal shelf sea-air CO_2 flux based on limited observed systems and using an up-scaling scheme. *Borges* [2005] showed that the inclusion of the coastal ocean increases the estimates of CO_2 uptake by the global ocean by 57% for high latitude areas, and by 15% for temperate latitude areas, while at subtropical and tropical latitudes the contribution from the coastal ocean increases the CO_2 emission to the atmosphere from the global ocean by 13%. *Cai et al.* [2006] conducted a study of sea-air carbon exchange in ocean margins by grouping the numerous heterogeneous shelves into seven distinct provinces. Their results showed that the continental shelves are a sink of atmospheric CO_2 at mid-high latitudes (-0.33 Pg C yr^{-1}) and a source of CO_2 at low latitudes (0.11 Pg C yr^{-1}), with a

net uptake of -0.22 Pg C yr^{-1}. *Laruelle et al.* [2010] evaluated the exchange of CO_2 between the atmosphere and the global coastal ocean from a compilation of sea-air CO_2 fluxes scaled using a spatially-explicit global typology of continental shelves. Their computed sink of atmospheric CO_2 over the continental shelf areas (-0.21±0.36 Pg C yr^{-1}) is at the low end of the range of previous estimates (-0.22 to -1.00 Pg C yr^{-1}). *Laruelle et al.* [2010] also concluded that the sea-air CO_2 flux per surface area over continental shelves, -0.7±1.2 mol CO_2 m^{-2} yr^{-1}, is twice the value of the open ocean based on the most recent CO_2 climatology at the time. More recently [*Cai*, 2011] showed that the continental shelves are sinks of atmospheric CO_2 (~0.25 Pg C yr^{-1}, but still with large uncertainty), accounting for ~17% of open ocean CO_2 uptake (1.5 Pg C yr^{-1}, *Takahashi et al*., 2009). The largest uncertainty of these scaling approaches stems from the availability of CO_2 data to describe the spatial variability, as well as to capture the relevant scales of temporal variability.

Given that relatively large amounts of carbon are exchanged via the sea-air interface in coastal seas and continental shelves, the knowledge of the seasonal and interannual variability of the sea-air CO_2 flux in coastal oceans is a very important component of the carbon budget, which requires comprehensive regional studies. In general, the coastal ocean is characterized by a high variability in carbon cycling, which presents significant challenges in determining spatial and temporal integrals of relevant quantities, such as the sea-air CO_2 flux. Therefore, innovative methods are needed for scaling up relatively sparse field measurements, in this case surface ocean pCO_2, into the required temporal and spatial resolutions to effectively derive regional sea-air CO_2 flux estimates. One method for obtaining such regionally integrated fluxes is through the use of biogeochemical-circulation models, which can be evaluated using the sparse field measurements, and then used to compute the mean and variability associated with these regional

120 fluxes [*Hofmann et al.*, 2011]. Satellite data, because of their high temporal and spatial
121 resolution, provide another very promising asset to accomplish this goal. For example, *Lohrenz*
122 *and Cai* [2006] conducted a satellite ocean color assessment of sea-air fluxes of CO_2 in the
123 northern Gulf of Mexico. They used principal component analysis and multiple-regression to
124 relate the surface ocean pCO_2 to SST, salinity and chlorophyll and used retrieval of
125 corresponding MODIS-Aqua products to assess the regional distributions of pCO_2.
126 In this paper we use multiple regression analysis to relate surface ocean pCO_2 to
127 environmental variables (SST, surface salinity, and chlorophyll) and use the resulting equations
128 with inputs from corresponding satellite products to provide an assessment of the spatial and
129 temporal variability of the surface ocean pCO_2 and sea-air CO_2 flux for the North American east
130 coast. A brief description of the biological/physical setting of the study region is provided in
131 Section 2.0. The processing of *in situ* and satellite data sets and the development of regionally
132 specific empirical pCO_2 algorithms are described in Section 3.0. The algorithm evaluation and
133 the estimates of sea-air flux from the available pCO_2 binned data and algorithm are provided in
134 Section 4.0, as well as a sensitivity analysis of parameters that influence the surface ocean pCO_2
135 seasonal and interannual variability. Finally, we provide a summary and discussion of suggested
136 future work in Section 5.0.
137
138 **2.0 Physical and Biological Setting**
139 The temporal and spatial variability of the surface ocean pCO_2 on continental shelves are
140 influenced by a combination of physical and biogeochemical factors, including surface
141 temperature-driven solubility, biological processes, fall-to-winter vertical mixing, ocean
142 circulation, river runoff, and shelf-ocean exchange [*Wang et al*., 2013]. Here we provide a

143 summary of the physical and biological factors that are potentially important in shaping the pCO_2
144 variability in the North American east coast continental shelf.

145 The definition of the coastal ocean is elusive, as it can be related to bathymetry,
146 hydrography, or distance from shore; and some features, such as river plumes and coastal
147 biomass maxima, can be ephemeral. Community efforts to standardize this definition to a fixed
148 distance from shore, such as *Hales et al*. [2008] as adopted by the Surface Ocean CO_2 Atlas
149 (SOCAT; http://www.socat.info/), extend seaward from the North American continent beyond
150 what we feel represents the reach of coastal processes. As a result, we have used the outer
151 boundaries of the regions defined by *Hoffman et al*. [2008, 2011] to define the extent of the
152 coastal ocean. The North American east coast (Fig. 1) encompasses three large regions of diverse
153 physical and biological characteristics: the southeast U.S. continental shelf, also known as the
154 South Atlantic Bight (SAB), the northeast U.S. continental shelf, and the Scotian Shelf (SS).
155 Within the northeast U.S. continental shelf there are four sub-regions: the Middle Atlantic Bight
156 (MAB), Georges Bank (GB), Nantucket Shoals (NS), and the Gulf of Maine (GoM). For this
157 study we combined the GB and NS regions into a single region (GB+NS) for simplicity and
158 because these two regions share many similar physical and biogeochemical attributes [*Fox et al.*,
159 2005; *Shearman and Lentz*, 2004; *Thomas et al.*, 2003]. These North American continental shelf
160 sub-regions are defined in *Hofmann et al.* [2011] with the GB+NS region separated from the
161 GoM as in *Hofmann et al.* [2008]. The 58 coastal sub-regions shown in *Hofmann et al*. [2008]
162 were developed based on a combination of bathymetry, SST fronts, stratification, and biological
163 properties. For simplicity, here we consolidate the very fine regional domains into five major
164 sub-regions described above. However, we recognize that previous studies have adopted other
165 methods to identify regional domains [*Hales et al.*, 2008; *Hales et al.,* 2012]. For example, a self

166 organizing mapping method has been adopted to sub-regionalize the North American Pacific
167 Coast [*Hales et al.,* 2012]. The method relies on an artificial neural network to identify
168 biogeochemical regions within the target study area.

169 Our focus is on the continental shelf which we operationally define as depths less than
170 200 meters since the depth of the actual shelf break varies. Bathymetric variation in our study
171 area is large. Portions of GB and NS are only several meters below the sea surface, whereas in
172 the GoM and areas of the SS, water depths exceed 200 m. Our study area is also at the
173 'crossroads' of the north-flowing Gulf Stream and the southwest-flowing slope water-Labrador
174 current [*Rossby*, 1987]. *Chapman and Beardsley* [1989] suggest that glacial melt and runoff
175 from Western Greenland generates a buoyancy-driven coastal current that flows over the SS and
176 GB and eventually into the MAB. This coastal current is an important driver to the distribution
177 of the marine CO_2 system, including surface pCO_2 along its flow path [*Wang et al*., 2013], i.e.,
178 the Gulf of St Laurence, the SS, the GoM and the MAB. There is little exchange of water
179 between the MAB and SAB along the narrow shelf at Cape Hatteras. In the SAB, the Gulf
180 Stream is close to the shelf break and has a direct influence on the outer SAB shelf [*Signorini*
181 *and McClain*, 2007], readily identifiable by the warm and salty signature shown in seasonal
182 maps of sea surface temperature (SST), sea surface salinity (SSS), and chlorophyll (*Chl*) of Fig.
183 2 (see Section 3.0 for methodology), whereas north of Cape Hatteras, the influence of the Gulf
184 Stream is more indirect. Here anti-cyclonic warm core rings result from landward meanders of
185 the Gulf Stream [*Joyce et al.*, 1992]. The rings are carried in the southwestward flow of slope
186 water where they interact with the outer shelf from GB to Cape Hatteras, frequently entraining
187 phytoplankton-rich shelf water [*Joyce et al.*, 1992]. Near Cape Hatteras, the warm core rings
188 may be reabsorbed into the Gulf Stream, a process readily apparent in daily time series

189 animations of chlorophyll (*Chl*) and SST. In the SAB, the outer shelf waters are warmer (Fig. 2)
190 in summer and autumn than winter and spring due, in part, to the proximity of the Gulf Stream as
191 a result of the expansion of the subtropical gyre [*Signorini and McClain*, 2007].

192 The pCO_2 variability in riverine-plume systems is a result of complex biogeochemical
193 interactions. In the Gulf of Maine for instance, labile riverine carbon is responsible for sustaining
194 supersaturated pCO_2 conditions in late fall, while at other times of the year phytoplankton
195 productivity, most likely driven by inputs of riverine dissolved inorganic nitrogen, is responsible
196 for pCO_2 undersaturation [*Salisbury et al.*, 2008]. The North American east coast continental
197 shelf is influenced by the discharge of several major rivers and estuaries (Chesapeake Bay,
198 Delaware Bay, and Gulf of St Lawrence, for example) that contribute to complex physical and
199 biogeochemical interactions that influence the seasonal and interannual variability of the surface
200 ocean pCO_2, an important parameter for the determination of the sea-air CO_2 flux. *Vandemark et*
201 *al*. [2011] showed that the observed pCO_2 and CO_2 flux dynamics in the Gulf of Maine are
202 dominated by a seasonal cycle, with a large spring influx of CO_2 and fall-to-winter efflux back to
203 the atmosphere. They also showed that in the western Gulf of Maine the ocean is a net source of
204 carbon to the atmosphere (+0.38 mol CO_2 m^{-2} yr^{-1}) over a period of five years, but with a
205 moderate interannual variation where years 2005 and 2007 represent cases of regional source
206 (+0.71 mol CO_2 m^{-2} yr^{-1}) and sink (-0.11 mol CO_2 m^{-2} yr^{-1}) anomalies, respectively. Comparison
207 of results with the neighboring Middle Atlantic and South Atlantic Bight shelf systems showed
208 that the Gulf of Maine differs by enhanced pCO_2 control factors other than temperature-driven
209 solubility, such as biological drawdown, fall-to-winter vertical mixing, and river runoff
210 [*Salisbury et al.*, 2008; *Shadwick et al.*, 2010].

Shadwick et al. [2011] investigated the seasonal variability of pCO_2 in the Scotian Shelf and concluded that the region acts as a net source of CO_2 to the atmosphere on an annual basis (1.4 mol CO_2 m^{-2} yr^{-1}). On a seasonal basis, there is a reversal of the flux only when a pronounced undersaturation of surface waters is reached for a short period during the spring bloom. Outside of the spring bloom period, the competing effects of temperature and biology influence on surface pCO_2 are nearly equal and opposite. *DeGrandpre et al.*[2002], based on measurements of surface ocean pCO_2 during the Ocean Margins Program [*Verity et al.*, 2002], concluded that the MAB is a sink of atmospheric CO_2 with an annual mean of -1.0 ± 0.6 Tg C yr^{-1}, or an area average of -1.1 ± 0.7 mol CO_2 m^{-2} yr^{-1}. A significant portion of this atmospheric uptake is a result of the annual cycle of heating and cooling combined with strong winds during the winter undersaturation period.

Jiang et al. [2008] showed that on an annual basis the SAB is a relatively small net sink of atmospheric CO_2 (-0.48 ± 0.21 mol CO_2 m^{-1} yr^{-1}). Seasonally, the SAB shifts from a sink of atmospheric CO_2 in winter to a source in summer. The annual cycle of sea surface temperature plays an important role in controlling the seasonal variation of pCO_2. The combination of stronger wind speeds during fall-winter, when CO_2 undersaturation is significant due to lower SSTs, results in a net annual CO_2 sink. Other important factors controlling the pCO_2 variability in the SAB are the marsh export of organic carbon and DIC in the warm months (June-November), which directly supports CO_2 outgassing in these months via organic carbon decomposition and increase in DIC [*Jiang et al.*, 2013; *Wang et al*., 2005]. In addition, the marsh areas in the SAB also export alkalinity, another important factor influencing the variability of pCO_2 and sea-air flux [*Wang et al.*, 2005; *Wang and Cai*, 2004].

233 The seasonal *Chl* climatology from MODIS Aqua (Fig. 2) shows that the maximum *Chl*
234 in the GoM, GB and NS occurs during spring (March-April-May, MAM). The GB region has the
235 highest *Chl* in spring, but it is maintained at concentrations above 2.5 mg m^{-3} in all seasons due
236 to vigorous tidal mixing. Fig. 2 also shows that the low-salinity nearshore waters along the entire
237 east coast coincide with regions of elevated *Chl*, an indication of the influence of nutrient-rich
238 riverine waters. On the MAB shelf, there is a high-*Chl* region during winter (December-January-
239 February, DJF) in the near shore and outer-shelf waters, but the fall bloom (SON) dominates
240 between approximately the 40- and 60-m isobaths. The high satellite-derived '*Chl*' in winter may
241 be in part colored dissolved organic matter flowing out from rivers, plus photo-acclimation by
242 phytoplankton (higher *Chl-a* due to low surface solar radiation and a well-mixed water column).
243 The minimum surface *Chl* over much of the MAB occurs during summer (JJA) when
244 highest SST (Fig. 2), peak stratification and a pronounced subsurface *Chl* maximum layer occur
245 [*O'Reilly and Zetlin*, 1998]. Summer mixed-layer depths of ~3.5 to 10 m are typical for MAB
246 shelf waters. The spring bloom (MAM) is clearly shown by the elevated *Chl* concentrations in
247 the MAB, GB, and GoM (Fig. 2). Fig. 2 also shows that the SAB *Chl* has its largest changes in
248 the outer shelf, with a maximum in DJF and lowest values in JJA under the influence of the
249 oligotrophic waters of the Gulf Stream.
250
251 **3.0 Data Sets and Methods**
252 3.1 Processing of *In Situ* and Satellite Data Sets
253 The surface ocean pCO_2 data are obtained from SOCAT, combined with additional
254 available data from regionally specific field experiments (see Appendix A) and binned by month
255 for each year (1978-2010) into 0.15^{o}x0.15^{o} grid cells. The SOCAT data [*Pfeill et al.*, 2012] holds

256 6.3 million quality-controlled surface ocean pCO_2 from the global oceans and coastal seas
257 covering the period of 1968 to 2007. These data were put together following uniform format and
258 a strict protocol that included quality control with clearly defined criteria performed by a team of
259 international experts.

260 The MatLab function bin2d, developed by *J. Nielsen* and available at the Nansen
261 Environmental and Remote Sensing Center (NERSC) from www-2.nersc.no/~even/, was used to
262 bin all data sets into the study grid. First, all the available data within 24^{o}N to 46^{o}N and 82^{o}W to
263 56^{o}W were selected for binning. These included 416,261 co-located surface ocean pCO_2, SST
264 and sea surface salinity (SSS) values from SOCAT from the period 1978-2007, 11,628 from the
265 2006 SAB cruise (only 2005 cruises are included in SOCAT), and 309,665 from the GoM (2004-
266 2010). The binned pCO_2 data were then adjusted to reference year 2004 using an atmospheric
267 growth rate of 1.68 μatm yr^{-1} [*Le Quéré et al.*, 2010] and assuming that the surface ocean pCO_2
268 is trending at the same pace as the atmosphere. All the adjusted pCO_2 data were then binned into
269 12 individual calendar months, each containing the average of all data within a particular month
270 and grid bin. The data were then divided into regional study domains following the boundaries
271 shown in Fig. 1.

272 The available pCO_2 data were divided into two individual sets, one dedicated to
273 algorithm development (data bins covering more than 6 months) and one dedicated to algorithm
274 evaluation (data bins covering less than 6 months). Surface ocean pCO_2 data from underway
275 (UW) transects across the Scotian Shelf and pCO_2 time series from the CARIOCA buoy located
276 at 44.296^{o}N and 63.257^{o}W [*Shadwick et al.*, 2010] were also used for algorithm evaluation,
277 together with SOCAT data on the Scotian Shelf not used for the algorithm development. Fig. 3a
278 shows color-coded SOCAT surface ocean pCO_2 cruise tracks and Fig. 3b shows corresponding

coastal binned data with associated color-coded temporal coverage in months. The highest temporal coverage corresponds to the most travelled routes (in orange to red), i.e., most frequent destination ports (Boston, New York, Norfolk, Miami) used by the Volunteering Observing Ships (VOSs). The VOS ships according to map available at the CDIAC web site (http://cdiac.ornl.gov/oceans/VOS_Program/) are: the Skogafoss, A. Companion, Oleander, Falstaff, and Explorer of the Seas. The SOCAT data set also includes transects occupied by research vessels. Fig. 3 clearly shows that the surface ocean pCO_2 data have spatial and temporal distribution gaps that may be potentially responsible for biases in the calculation of sea-air fluxes.

Monthly sea-surface salinity (SSS) climatology was interpolated and gridded onto the 0.15^{o}x0.15^{o} study domain grid using the World Ocean Database (WOD) 2009 station data and the method of Kriging. The Interactive Data Language (IDL) function KRIG2D was used for this purpose. Monthly climatologic mixed layer depth (MLD) was derived from WOD 2005 for the entire East Coast based on temperature profiles using 0.5^{o} C temperature difference criterion [*Hofmann et al.*, 2008]. The MLD data were binned into the same 0.15^{o}x0.15^{o} study domain grid.

Both data and algorithm sea-air CO_2 flux estimates were obtained using gridded (0.25^{o}x0.25^{o}) winds from the Jet Propulsion Laboratory Cross-Calibrated Multiple Platforms (CCMP, *Atlas et al*., 2011) product (ftp://podaac-ftp.jpl.nasa.gov/allData/ccmp/L2.5/flk). Monthly wind climatology was derived using data from 1999 to 2008, a period approximately centered on 2004, the reference year adopted for the adjusted surface ocean pCO_2 data. The climatologic and interannual CCMP monthly winds were re-gridded (0.15^{o}x0.15^{o}) and extrapolated nearshore using the function “surface” from Generic Mapping Tools (GMT, *Smith*

302 *and Wessel*, 1990; *Wessel and Smith*, 1991) which is based on an adjustable tension continuous
303 curvature surface gridding method. High frequency (10-minute) winds from 10 NOAA National
304 Oceanographic Data Center NDBC buoys (http://www.nodc.noaa.gov/BUOY/) and hourly winds
305 from Sable Island were used to obtain correction coefficients to account for nonlinearities in the
306 gas exchange parameterization resulting from the use of monthly climatologic winds. The
307 method for deriving these coefficients is described under sub-section 3.3.

308 All parameters used to develop the pCO_2 algorithm and to derive the sea-air CO_2 flux,
309 including all satellite data products (SST and *Chl*), SSS and the CCMP wind speed were also
310 binned monthly into the same grid. The satellite data products consisted of 9-km, level 3
311 mapped, MODIS Aqua (MODISA) climatologic and interannual monthly composites of SST and
312 *Chl* obtained from the NASA ocean color distribution archive (http://oceancolor.gsfc.nasa.gov/).
313 A validation between log-transformed MODISA *Chl* retrievals vs. all available *in situ*
314 observations (SAB to GoM, depth<=200m, N=404), conducted using the SeaBASS (SeaWiFS
315 Bio-optical Archive and Storage System: http://seabass.gsfc.nasa.gov/) data search and
316 validation tools, showed good matchup agreement (r^2=0.75, RMSE=0.30, APD=35.8%). For the
317 algorithm development we used the available binned surface ocean pCO_2, SST and SSS derived
318 from the *in situ* data, combined with monthly climatologic satellite *Chl* binned at the same grid
319 points as no *in situ* concurrent *Chl* measurements are available. For the algorithm application we
320 used monthly interannual (2003-2010) satellite SST and *Chl*, and monthly climatologic SSS
321 derived from WOD 2005 data.

322 Seasonal maps were constructed by averaging the monthly data and derived products into
323 four three-month composites, defined as: winter (December-January-February, DJF), spring

(March-April-May, MAM), summer (June-July-August, JJA), and autumn (September-October-November, SON).

3.2 Development of Regional pCO_2 Algorithms

The algorithm development is based on binned *in situ* pCO_2, SST and SSS, and satellite-derived *Chl* monthly climatology, as well as day of the year (Julian day). The algorithm was developed through the multiple linear regression (MLR) analysis based on all spatial bins containing more than six available monthly occurrences of the *in situ* data (remaining data were reserved for evaluation), and is represented as:

$$pCO_2 = [a + bDay' + c(T - T_o) + d(S - S_o) + e[log_{10}(Chl) - log_{10}(Chl_o)]+ 1.68(year - 2004) \quad (1)$$

$$\text{where,} \qquad Day' = \cos\left(\frac{2\pi(Day - \gamma)}{365}\right)$$

The first terms in brackets represent the surface ocean pCO_2 corrected to the year 2004 and the last term is a correction factor for different years to account for the rise of surface ocean pCO_2 due to the uptake of anthropogenic CO_2. The input for ''*Day*'' (Julian day) was normalized sinusoidally (Day') to emphasize the seasonal cycle and to allow January to be close to both February and December [*Friedrich and Oschlies*, 2009; *Lefèvre et al.*, 2005]. The value of γ (phase of *Day*' in days) is optimized via iteration (ranging from 0 to 365 days) until the minimum RMSE is obtained. T_o, S_o, Chl_o are temperature, salinity, and chlorophyll mean values for each region. The choice of $log_{10}(Chl)$ instead of *Chl* in our algorithm was an arbitrary choice, and therefore limited mechanistic information can be drawn in the empirical result.

346 A separate analysis was conducted to evaluate the algorithm by using surface ocean pCO_2
347 data not used in the development of the algorithm equations (see Section 4.1). These data
348 consisted of bins from the monthly composites that have less than six months of available pCO_2
349 occurrences. Satellite-derived SST, *Chl*, *in situ* SSS monthly climatology was matched with the
350 locations and months of the selected pCO_2 bins and used as algorithm input. The pCO_2 derived
351 from the algorithm (pCO_2^{fit}) was matched with the observed pCO_2 (pCO_2^{obs}) and a scatter plot
352 and histogram of residuals were made for all combined regions to evaluate the algorithm
353 performance. The algorithm was also evaluated using data from the SS (*Shadwick et al*., 2010).
354
355 3.3 Calculation of the Sea-air CO_2 Flux
356 The sea-air pCO_2 difference (ΔpCO_2) was calculated using monthly GLOBALVIEW
357 [GLOBALVIEW-CO2, 2011] atmospheric xCO_2 from Grifton, North Carolina, a station located
358 approximately midway in the study domain. The xCO_2 (in μmol mol^{-1}) was converted to pCO_2
359 (air) using the method of *Jiang et al.* [2008]. For this conversion we used monthly surface
360 barometric pressure and air temperature from NOAA NCEP-NACR CDAS-1 [*Kalnay et al*.,
361 1996] and monthly climatologic SSS from WOA09. Although several other GLOBALVIEW
362 stations are available along the study coastal domain, the atmospheric pCO_2 records are not very
363 different to justify a more site-specific use of the data. Regarding the use of the atmospheric
364 xCO_2 in this study, it has been demonstrated that there are uncertainties involved in using marine
365 boundary layer xCO_2 rather than the *in situ* xCO_2 due to the effect of continental processes. For
366 example, *Jiang et al*. [2007] showed that the average atmospheric xCO_2 on the SAB can be
367 almost 10 ppm higher than the measured in the open ocean with the potential of reversing the
368 direction of the sea-air flux. Although this is a potential source of uncertainty in the calculation

of the sea-air flux, concurrent *in situ* atmospheric xCO_2 are only available for a limited number of coastal cruises.

Climatologic (1999-2008) CCMP monthly wind speeds at 10-m anemometer height (U_{10}), based on a decade of data centered on the reference year 2004, were binned similarly and used to derive the monthly sea-air CO_2 flux for each bin and each month using the following gas transfer parameterization

$$Flux = k_{660}(\frac{Sc}{660})^{-1/2}\, s\, \Delta pCO_2 \qquad (2)$$

in units of mol CO_2 m^{-2} d^{-1}. *Sc* is the Schmidt number (non dimensional), *s* the solubility of CO_2 in seawater in mol CO_2 m^{-3} μatm^{-1}, and ΔpCO_2 is the sea-air pCO_2 difference in μatm. The term k_{660} is the quadratic gas transfer coefficient in cm h^{-1} (converted to m d^{-1}). We calculated the sea-air CO_2 flux using two relationships of gas exchange with wind speed (U_{10}), the quadratic dependence formulation of *Ho et al.* [2011], for which $k_{660} = 0.262 C_2 U_{10}^2$, and the polynomial dependence of *Wanninkhof et al.* [2009], for which $k_{660} = 3 + 0.1U_{10} + 0.064 C_2 U_{10}^2 + 0.011 C_3 U_{10}^3$, using the appropriate nonlinearity correction coefficients C_2 and C_3, which are correction factors to account for the use of monthly climatologic wind speeds [*Jiang et al.*, 2008]. These were calculated using 10-minute wind speeds from 10 NDBC buoys distributed within the SAB, MAB, GB+NS, and GoM regions, and Sable Island 1-hour wind speeds for the SS (see locations in Fig. 1), and the correction factor equations given in *Jiang et al.* [2008] , $C_2 = \left(\frac{1}{n}\sum_j^n U_j^2\right)/U_{mean}^2$ and $C_3 = \left(\frac{1}{n}\sum_j^n U_j^3\right)/U_{mean}^3$, where U_j is the high-frequency wind speed (m/s), U_{mean} is the monthly mean wind speed (m s^{-1}), and n is the number of available wind speeds in each month. The value of C_2 and C_3 were obtained for each site and month for the

period 1999-2008. Monthly climatologic averages were calculated for each site and for each region. The values of C_2 range from 1.2 to 1.3, while those for C_3 range from 1.6 to 2.0. These values were then used to apply corrections to the gas transfer parameterizations when calculating the sea-air CO_2 flux. The same methodology was applied to derive data-based and algorithm-based sea-air fluxes. We use the atmospheric convention for the CO_2 flux, i.e., a negative flux is defined as a sink of atmospheric CO_2 by the ocean.

The regional algorithms (Table 1 and Equation 1) were used to derive values of surface ocean pCO_2 using MODIS Aqua monthly composites of SST and *Chl* for 2003-2010, and monthly SSS climatology. Gap filling of missing satellite data was done with monthly climatology composites for each of the input parameters. The sea-air CO_2 flux was then computed using interannual monthly CCMP winds and the gas transfer parameterization shown in Equation 2.

3.4 Monthly Climatology of DIC and Alkalinity for pCO_2 Parameter Sensitivity

The data sets used to generate monthly climatologies of DIC and alkalinity (Alk) include the MODIS SST monthly climatology, the Kriged monthly SSS climatology derived from WOA 2009 salinity data, and surface ocean pCO_2 from the algorithm. Monthly alkalinity was derived as a function of salinity from *Cai et al.* [2010] using SSS monthly climatology. DIC was then derived from alkalinity, SST, SSS, and monthly pCO_2 from the algorithm using CO2SYS (http://cdiac.ornl.gov/ftp/co2sys/CO2SYS_calc_MATLAB/), a MatLab program to calculate the state of the carbonate system. The input for CO2SYS consisted of alkalinity, DIC, SST, SSS, the choice of H_2CO_3 and HCO_3^- dissociation constants (K_1, K_2) of "Mehrbach refit" [*Dickson and Millero*, 1987], the choice of HSO_4^- dissociation constant of " Dickson" [*Dickson*, 1990], and

415 zero concentration for silicate and phosphate. The total borate-salinity relationship of *Uppstrom*
416 [1974] was used.

417 The monthly binned SST, SSS, DIC, and alkalinity fields were then averaged over each
418 region to obtain 12 monthly values for each variable and region. We refer to these regional
419 averages as SST^i, SSS^i, DIC^i, and Alk^i, where the superscript indicates the calendar month from
420 1 to 12. We also computed the annual average of each of these four spatial averages, which we
421 call, $\overline{SST}$, $\overline{SSS}$, $\overline{DIC}$, and $\overline{Alk}$. From the regional averages, we computed the monthly pCO_2 using
422 CO2SYS,

423 $$pCO_2^i = pCO_2\,(SST^i, SSS^i, DIC^i, Alk^i), \quad (3)$$

424 and the annual average, $\overline{pCO_2}$.

425 The deviation of pCO_2 from its annual average is given by

426 $$\delta^i = pCO_2^i - \overline{pCO_2} \quad (4)$$

427 To determine the sensitivity of pCO_2 to each of the four variables, we hold three variables
428 at their annual averages and let the fourth variable change from month to month. For example, to
429 determine the impact of temperature on pCO_2, we computed

430 $$pCO_2^{i,SST} = pCO_2(SST^i, \overline{SSS}, \overline{DIC}, \overline{Alk}) \quad (5)$$

431 In an analogous way, we computed $pCO_2^{i,SSS}$, $pCO_2^{i,DIC}$, and $pCO_2^{i,Alk}$, which describe
432 the respective influences of SSS, DIC, and Alk on pCO_2. We also computed the deviation of
433 pCO_2 from its annual average due to each of the four variables. For example, the deviation of
434 pCO_2 from its annual average due to temperature is $\delta^{i,SST} = pCO_2^{i,SST} - \overline{pCO_2}$. Similarly, $\delta^{i,SSS}$,

435 $\delta^{i,DIC}$, and $\delta^{i,Alk}$, describe the deviations of pCO_2 from its annual average due, respectively, to

436 SSS, DIC, and Alk. The results of this analysis will be discussed in sub-section 4.3.

437

438 **4.0 Results and Discussion**

439 Regional algorithms were developed with distinct coefficients derived for each of the five

440 regions (Table 1) and then used to derive seasonal and interannual surface ocean pCO_2 and sea-

441 air CO_2 fluxes (Tables 2 and 3).

442

443 4.1 Performance of Regional Algorithms

444 In this section we provide an assessment of the statistical importance of each proxy

445 parameter used in the algorithm (Fig. 4), regional matchups of algorithm versus data and

446 seasonal pCO_2 plots based on monthly averages derived from data and algorithm (Fig. 5),

447 algorithm versus data matchups using pCO_2 observations not used in the algorithm development

448 (Fig. 6), a regional matchup analysis for the Scotian Shelf (SS) using a combination of UW pCO_2

449 data from Dalhousie University and a few from SOCAT (Fig. 7), and time-series of algorithm

450 pCO_2 for seven distinct sub-regions of the SS (concurrent data points) following a more recent

451 work of *Thomas et al*. [2012] (Fig. 8). Finally, a high frequency algorithm validation was

452 performed against surface pCO_2 observations from the CARIOCA buoy on the SS using

453 concurrent hourly observations of SST, SSS, and *Chl* (Fig. 9).

454 Fig. 4 shows the statistical (goodness-of-fit) performance resulting from the incremental

455 addition of proxy parameters for each of the five regions. The statistical performance is shown as

456 a goodness-of-fit diagram with normalized RMSE on the *x*-axis, and $(1 - r^2)$ on the *y*-axis.

457 Consequently, a perfect fit would lie at the origin of this diagram (0, 0). The diagram shows that

458 the variable *Day*' by itself provides (1 - r^2) values less than 0.6 for all regions. Incremental
459 improvements of both normalized RMSE and (1 – r^2) are different for each region. Extreme
460 examples of statistical improvement are the addition of salinity for the SAB and $\log_{10}(Chl)$ for
461 the SS.

462 Fig. 5 shows scatter plots of algorithm-derived versus observed surface ocean pCO_2 and
463 associated seasonal plots of regionally-averaged pCO_2. As shown in Table 1, there is a statistical
464 range for the coefficients derived for each region using Equation 1. The r^2 is lowest for the GoM
465 (0.42) and highest for the SAB (0.82). The quality of the statistical fit depends on a combination
466 of factors, including data coverage and how well the proxy variables represent the surface ocean
467 pCO_2 variability in space and time within each region.

468 The regional algorithms were then applied using binned inputs (SST, SSS, and *Chl*)
469 matching the month and location of the observed surface ocean pCO_2 not used for the algorithm
470 development, and then compared with the corresponding observed pCO_2. The results are shown
471 in Fig. 6a and 6b. The observed versus algorithm correlation coefficient (color coded scatter plot
472 in Fig. 6a with summary of statistics in the legend) range from 0.27 (r^2) for the GoM with a
473 RMSE= 25 μatm to 0.78 for the SAB with a RMSE=21 μatm. The histogram of residuals (Fig.
474 6b) shows that 86% of the residuals are less than the observed pCO_2 standard deviation (±σ),
475 while 40% of residuals are within less than σ/3 (±16 μatm).

476 Data from SOCAT on the SS, and Dalhousie University UW transects [*Shadwick et al.,*
477 2010] covering the period of 2004-2008, were averaged within seven 2^ox2^o boxes on the SS (Fig.
478 7a) and compared with area-averaged algorithm predictions within the same boxes. The scatter
479 plot of observed vs. algorithm pCO_2 for the 37 resulting averages is shown in Fig. 7b. The
480 agreement between data and algorithm predictions is quite reasonable with r^2=0.79 and

RMSE=26.2 μatm. The time series of algorithm pCO_2 was obtained using SST and *Chl* from MODIS Aqua monthly composites and WOA09-derived SSS climatology. The algorithm time series for all seven boxes are shown in Figs. 8a and 8b with the SOCAT (red circles) and UW (blue circles) values superposed for comparison. A high frequency algorithm test was done by comparing the CARIOCA buoy one-hour pCO_2 record on the SS during 2007-2010 with algorithm results using one-hour inputs of SST, SSS and calibrated fluorometer *Chl* concurrent observations from the buoy. These data have been reported by *Thomas et al*. [2012]. The time series and scatter plot of observed vs. algorithm pCO_2 are shown in Fig. 9. The algorithm predictions track the observed pCO_2 reasonably well with r^2=0.46, RMSE=40.3 μatm and mean absolute percent difference (MAPD) of 8.8%. The observed and algorithm values for 2007-2010 mean and standard deviation are quite similar, 422.3±54.7 μatm and 413.1±56.9 μatm, respectively, which show a relatively small bias (9 μatm) and very similar variance.

4.2 Seasonal Surface Ocean pCO_2, Alkalinity, DIC and Sea-Air Flux from Data and Algorithm

Fig. 10 shows seasonal maps of algorithm surface ocean pCO_2 adjusted for reference year 2004 and corresponding seasonal maps of alkalinity and DIC. Fig. 10 shows that the temporal and spatial variability of pCO_2 is quite different from region to region and that the seasonal changes are not in sync among the five analyzed coastal domains. This is also evident in the seasonal plots of data-derived surface ocean pCO_2 in Fig. 5. The lowest values (280 to 320 μatm) occur mostly during winter (DJF) in the MAB, SAB, and in the near shore areas of the SS in spring (MAM). Low values are also present in spring in the GB+NS region. These low values are generally associated with low SSTs (See Fig. 2). The highest values (> 480 μatm) occur in the offshore region of the SS in autumn (SON) and the near shore areas of the SAB in summer

504 (JJA), the latter influenced by the discharge of carbon-rich (primarily DOC) estuarine effluents
505 [*Alberts and Takacs*, 1999; *Cai*, 2011] and marsh DIC export [*Wang and Cai*, 2004]. The surface
506 ocean pCO_2 in the MAB shows much less variability alongshore than cross-shelf, except in the
507 southern region and outer shelf where Gulf Stream intrusions and shelf-slope fronts induce
508 strong hydrographic and biogeochemical horizontal gradients. *DeGrandpre* [2002], and
509 references within, identified similar alongshore homogeneity in connection with little alongshore
510 variability on mid-shelf hydrography, nutrients, surface dissolved oxygen, *Chl* concentrations,
511 and primary production. The high values in the offshore region of the SS in autumn are
512 associated with low drawdown by phytoplankton, as indicated by the higher values of DIC, as
513 shown in Fig. 10 discussed later in this section, and confirmed by the work of *Craig et al.* [2013]
514 for this region. The GoM has highest pCO_2 (> 400 μatm) values in winter and fall when vertical
515 mixing is more vigorous and phytoplankton drawdown is significantly reduced.
516 The seasonal maps of alkalinity in Fig. 10 follow the seasonal surface salinity distribution
517 in Fig. 2 as alkalinity was derived as a linear function of salinity, albeit with different
518 coefficients for each region. There is a sharp transition in alkalinity at Cape Hatteras. South of it,
519 in the SAB, alkalinity is highest in the middle and outer shelves due to the influence of high-
520 salinity Gulf Stream waters. Alkalinity is highly reduced in the nearshore region under the
521 influence of low-salinity riverine waters. However, in the very nearshore areas high alkalinity
522 values were observed due to significant export from the marsh areas during the warm months
523 [*Cai et al.*, 1998]. North of Cape Hatteras all regions have much lower alkalinity than the middle
524 and outer shelf regions of the SAB. The inner and middle shelf regions of the MAB and southern
525 GoM have even lower alkalinity, especially during summer (JJA) when surface salinity is at a
526 minimum. This summer minimum salinity follows the peak discharge of the major rivers in

527 spring with a delay of approximately 1-2 months [*Whitney*, 2010]. However, the SSS minimum
528 on the SS comes in autumn (SON) with the peak St Lawrence outflow.

529 The Alk and salinity relationships generally followed a single river-ocean mixing line in
530 the SAB and MAB regions, but a two-segment line in the northeastern waters due to the strong
531 alongshore current and influences from the low alkalinity local rivers [*Cai et al*., 2010].

532 The seasonal DIC maps in Fig. 10 show highest values in the GoM and offshore regions
533 of the SS in winter-spring, a likely result of vigorous vertical mixing. Lowest DIC values occur
534 in the MAB and southern GoM in summer, influenced by the low-DIC riverine waters that peak
535 during spring, as well as low-DIC water of the Labrador Coastal Current that flows through the
536 region [*Wang et al*., 2013]. The DIC seasonal variability is also highly influenced by the
537 drawdown of CO_2 by the net community production during spring-summer. In general, the SAB
538 has much less seasonal DIC and alkalinity variability than the other regions to the north.

539 The monthly and annual mean sea-air CO_2 flux was calculated using ΔpCO_2 derived from
540 both binned data and algorithm (Table 2) and the two gas transfer parameterizations described in
541 Section 3.3. The estimates were based on monthly wind climatology for 1999-2008 derived from
542 satellite (Atlas CCMP) winds. The differences between the two different parameterizations are
543 relatively small ranging from 6% to 17%, except for the GoM where the fluxes are small causing
544 much larger differences between the two methos. For simplicity we compare the flux estimates
545 between binned data and algorithm based on the *Ho et al*. [2011] parameterization.

546 There is a general agreement in sign and magnitude between the data-derived and
547 algorithm-derived estimates for the MAB, SAB, and GB+NS (Table 2). The annual mean sea-air
548 CO_2 flux in the GoM derived by both methods range from +0.02±0.12 to +0.17±0.32 Tg C yr^{-1},
549 or a weak source to the atmosphere on average, but within the range of the estimates given by

550 *Vandermark et al*. [2011] for the southern GoM (-0.16 to +1.1 Tg C yr^{-1} when converted from
551 specific to up-scaled total sea-air flux for the entire GoM). The MAB, SAB, GB+NS and SS are
552 net sinks ranging from -0.6±0.2 to -1.8±0.2 mol CO_2 m^{-2} yr^{-1}. These estimates from the binned
553 data and algorithm are in general agreement with previous studies (see Table 2) when the range
554 of uncertainty and interannual variability are taken into account. One exception is the SS where
555 previous studies [*Shadwick et al*., 2010; *Shadwick et al.*, 2011] indicate that the SS is a source of
556 CO_2 to the atmosphere while this study indicates the opposite. Since the algorithm seems to
557 perform well in the SS when compared with the available data, the reason(s) for the apparent
558 discrepancy remains elusive and highlights the fact that there are still large differences in the sea-
559 air flux estimates with different degrees of uncertainty from region to region.
560 The combined uptake by the east coast continental shelf based on both binned data and
561 algorithm, and using both gas transfer parameterizations, ranges from 3.6 to 4.3 Tg C yr^{-1}.
562
563 4.3 Sensitivity Analysis of Parameters that Influence the pCO_2 Seasonal Variability
564 Here we present a sensitivity analysis of the most influential parameters affecting the
565 surface ocean pCO_2 variability in the study region. The seasonal cycles of each influential
566 parameter are plotted in Fig. 11 together with the seasonal surface ocean pCO_2 from the
567 algorithm with the seasonal mean removed. Inspection of Fig. 11 shows that the amplitude of
568 SST and DIC contributions in the MAB, GoM, GB+NS, and SS are similar but having opposite
569 phase. Seasonal variability of pCO_2 (DIC) in these regions is consistent with winter mixing
570 enhancement and biological drawdown in spring-summer. In contrast, the major contributing
571 factor to the seasonal pCO_2 variability in the SAB is SST. Alkalinity influence is the third most
572 important and salinity relatively the least influential. However, salinity has an impact in the

573 statistical improvement of the pCO_2 algorithm, most pronounced in the SAB, which is a region
574 where seasonal SSS variability is large (see Fig. 2), especially on the inner shelf.
575 The seasonal DIC variability averaged for all five study regions, with the MLD
576 superimposed, is shown in Fig. 12. The four study regions north of Cape Hatteras (MAB, GoM,
577 GB+NS, and SS) have distinct DIC seasonal cycles with amplitudes of 100 to 120 μmol kg^{-1}.
578 Regionally-averaged winter MLDs range from 30 m in the MAB to more than 100 m in the
579 GoM. Deeper MLDs in winter/autumn, resulting from wind and convective mixing, is the major
580 factor contributing to the elevated DIC concentrations (2010 to 2080 μmol kg^{-1}) shown during
581 these seasons. The shoaling of the MLDs in spring-summer, together with the drawdown of CO_2
582 by biology, are the major factors driving the significant reduction in surface DIC. For instance, in
583 the MAB the DIC drops from 2020 μmol kg^{-1} in February-March to 1900 μmol kg^{-1} in June. In
584 addition to biology and deep mixing, DIC, and consequently the surface ocean pCO_2, is also
585 affected by sea-air exchange. In the GoM, for instance, there is a significant effect of the sea-air
586 exchange on DIC when the ΔpCO_2 is high and the mixed layer becomes very shallow (*J.*
587 *Salisbury* personal communication, 2012). The amplitudes of the seasonal MLD and DIC in the
588 SAB are significantly less than in the other regions, most probably due to the shallower depths
589 and much lower phytoplankton productivity.
590
591 4.4 Interannual Variability of Surface Ocean pCO_2 and Sea-Air Flux
592 The interannual variability of surface ocean pCO_2 and sea-air CO_2 flux were calculated
593 using the algorithm (Equation 1) with inputs from monthly satellite products (SST and *Chl*) for
594 2003-2010 and climatologic SSS. The sea air flux was computed using monthly CCMP winds
595 for the same period. The results are shown in Fig. 13 (pCO_2 left panel, sea-air flux right panel)

596 and summarized in Table 3. Note that the algorithm results in Table 2 were derived using
597 monthly satellite climatology of SST and *Chl*, and climatologic winds, while those in Table 3 are
598 from monthly interannual satellite products and winds. The GoM and SS have the largest
599 interannual variability in sea-air CO_2 flux. The flux in the SS is positive (source) in 2005 (+0.15
600 Tg C yr^{-1}) and negative (weak sink) in 2006 (-0.02 Tg C yr^{-1}), while the largest flux (-1.55 Tg C
601 yr^{-1}) occurred in 2007. These large differences in the SS annual fluxes are a result of large
602 interannual changes in the spring drawdown of surface ocean pCO_2 (see Fig. 13). However, in
603 the GoM the large differences in annual flux (+0.17 Tg C yr^{-1} in 2004 and -0.19 Tg C yr^{-1} in
604 2007) are a result of wind speed variability as there are not significant interannual changes in the
605 surface ocean pCO_2 seasonal cycle, as shown in Fig. 13.
606 Averaged over the entire eight years, the MAB, GB+NS, and SAB are relatively the
607 largest sinks of CO_2 to the atmosphere (-2.1, -1.0, and -0.9 Tg C yr^{-1}, respectively), while the
608 GOM is a small source (+0.01 Tg C yr^{-1}) and the SS a relatively small sink (-0.6 Tg C yr^{-1}),
609 albeit with large changes from year to year. The east coast uptake (mean over the 8 years) is 4.6
610 Tg C yr^{-1}, which is at the upper end of the estimates from the binned field measurements with
611 two different gas transfer parameterizations (4.0 to 4.3 Tg C yr^{-1}), and 3.6 to 4.0 Tg C yr^{-1} from
612 the algorithm using monthly climatology inputs (see Table 2). Table 3 shows that the lowest
613 estimate occur in 2006 (3.4 Tg C yr^{-1}) and the highest in 2007 (5.4 Tg C yr^{-1}).
614 The interannual variability in sea-air flux in all regions is mostly due to changes in the
615 surface ocean pCO_2, mainly in response to changes in solubility and biological drawdown due to
616 variability in SST and phytoplankton production, respectively, and the wind-dependent gas
617 exchange at the sea-air interface, accounted for by the gas transfer coefficient k_{660} (in cm hr^{-1}).
618 From Table 1 we see that the algorithm pCO_2 sensitivity to the input parameters varies

619 significantly from region to region. In fact, the coefficients of many parameters change sign on a
620 regional basis. So, in order to evaluate which parameters influenced the resulting estimates of
621 sea-air flux the most, one needs to examine the yearly changes of these parameters and evaluate
622 how much influence they have on the pCO_2. As an example, there was a significant shift in the
623 mean annual sea-air flux in the SS from 2005 to 2007 (Table 3 and Fig. 14). In 2005 the SS was
624 a weak source of atmospheric CO_2 (+0.15 Tg C yr^{-1}), while in 2007 it shifted to a relatively
625 strong CO_2 sink (-1.55 Tg C yr^{-1}). This shift was associated with lower SST (-0.8 ^oC), higher
626 $\log_{10}[Chl]$ (+0.067), and higher k_{660} (+2.19 cm hr^{-1}) on average in 2007 compared to 2005. Using
627 the coefficients for SS in Table 1, 8.77 ± 0.26 μatm $(^oC)^{-1}$, -100.32 ± 4.66 μatm $(\log_{10}[Chl])^{-1}$, we
628 get the following changes in pCO_2 in 2007 compared to 2005: -7.1 ± 0.2 μatm from SST and -6.7
629 ± 0.3 μatm from *Chl*, for a total decrease in surface ocean pCO_2 of -13.8 ± 0.4 μatm. Considering
630 that this is a regionally and annually averaged value, this is a significant change in pCO_2 , which,
631 combined with the increase in $k_{660,}$ is the main reason leading to changes in sea-air flux.
632 Time series (2003-2010) of annual mean sea-air CO_2 flux averaged for each of the five
633 regions, each combined with annual means of SST, $\log_{10}[Chl]$, and k_{660}, are shown in Fig. 14.
634 We show $\log_{10}[Chl]$ instead of absolute *Chl* concentration because the log-transformed *Chl* is the
635 parameter used by the algorithm. Examination of each of these time series reveals some
636 interesting interannual changes. The scale of variability for each variable changes from region to
637 region and it is reflected by adopting different vertical axis ranges for each region. Interestingly,
638 2006 is a year of transition for all regions north of Cape Hatteras (MAB, GB+NS, GoM, and SS).
639 In 2006, the highest SST and *Chl* occur in the GoM and SS, followed by a decrease in SST
640 reaching a minimum in 2007, which, combined with a peak in k_{660} resulted in the largest uptake
641 of CO_2 by the ocean in these two regions. As a result, there was a transition in the sea-air flux in

642 the SS from a very weak sink in 2006 (-0.02 Tg C yr^{-1}) to a stronger sink in 2007 (-1.55 Tg C
643 yr^{-1}). There was an increase of SST from 2007 to 2010 that contributed to a reduction in the
644 ocean uptake. The sea-air flux interannual variability in the GB+NS, MAB, and SAB was also
645 largely driven by changes in SST, with warmer years having reduced ocean uptake and colder
646 years showing an increase in uptake.

647 The annual mean time series of sea-air flux for each region (2003-2010), and the total for
648 the entire east coast, are shown in Fig. 15. The GoM and SS regions were relatively stronger
649 sinks of CO_2 to the atmosphere in 2007 (-0.19 and -1.55 Tg C yr^{-1}, respectively). The annual
650 uptake of CO_2 ranged from -0.51 to -1.12 Tg C yr^{-1} in the SAB with a mean of -0.89 ± 0.18 Tg C
651 yr^{-1} for 2003-2010. The equivalent values for the GB+NS were similar, with a range of -0.73 to
652 -1.20 Tg C yr^{-1} and an overall mean of -1.00 ± 0.18 Tg C yr^{-1}. The MAB was the largest sink
653 with values ranging from -1.73 to -2.43 Tg C yr^{-1}, and an overall mean of -2.12 ± 0.24 Tg C yr^{-1}.
654 The total sea-air flux (sum of all five regions) ranged from -3.4 to -5.4 Tg C yr^{-1}, with the lowest
655 uptake in 2006 and the highest in 2007.
656

657 **5.0 Summary and Future work**

658 We reconstructed a monthly climatology of surface ocean pCO_2 for the North American
659 east coast continental shelf and developed regional algorithms to analyze the seasonal and
660 interannual variability of surface ocean pCO_2 and sea-air CO_2 flux. A sensitivity analysis of
661 parameters that influence the surface ocean pCO_2 showed that changes in DIC and SST are the
662 main drivers for the pCO_2 seasonal cycle. Vertical mixing, mixing of low-salinity waters with
663 shelf water, and biological drawdown are highly influential in the DIC variability. Much larger
664 seasonal cycle amplitudes of DIC occur in regions north of Cape Hatteras than south of it. The

665 annual sea-air CO_2 flux for the entire East Coast derived from the algorithm ranges from -3.4 Tg
666 C yr^{-1} (2006) to -5.4 Tg C yr^{-1} (2007) during the analyzed period (2003-2010). In general,
667 estimates from the binned data and algorithm are in agreement with previous studies when the
668 range of uncertainty and interannual variability are taken into account.

669 Uncertainties in the estimates of sea-air flux can be reduced by filling the spatial and
670 temporal gaps in the existing surface ocean pCO_2 inventory for the US East Coast. The
671 limitations of spatial and temporal surface ocean pCO_2 data coverage present a challenge in
672 validating algorithms and biogeochemical model pCO_2 and sea-air flux estimates. Improvements
673 can only be obtained by continuous monitoring of pCO_2 and other carbon cycle related variables
674 in the near shore and shelf regions of the US East coast. As shown in Fig. 3, all regions have
675 major spatial and temporal gaps in the data coverage.

676 In this study, we used a multiple regression approach to convert regional satellite
677 observed quantities (SST, and *Chl*) into pCO_2. However, the relationship $pCO_2 = f$ (SST, *Chl*,
678 SSS, time) is empirical and does not represent a unique solution as pCO_2 depends on factors
679 other than local SST and *Chl,* for instance. Surface waters with identical SST and *Chl* can
680 possibly have different pCO_2 levels. However, there have been studies that apply the technique
681 of neural networks for mapping *in situ* pCO_2 data in the open ocean [*Friedrich and Oschlies*,
682 2009; *Lefèvre et al.*, 2005; *Telszewski et al.,* 2009]. The advantage of the neural network
683 approach is that it can recognize and exploit relationships in the data which are not pre-defined
684 (as in regression techniques) and need to be expressible by an equation. This makes neural
685 networks particularly suited to mapping relationships that are non-linear and empirical, provided
686 sufficient data are available to 'train' the network. This technique looks promising for mapping
687 the surface ocean pCO_2 in other coastal regions as well.

688 *Hales et al*. [2012] presented a method for predicting coastal surface-water pCO_2 from
689 remote-sensing data, based on self organizing maps (SOMs) and a nonlinear semi-empirical
690 model of surface water carbonate chemistry, a method potentially applicable to the coastal
691 regions in this study. The SOM approach was used to objectively map the sub-regions, while an
692 entirely different approach was used to develop the pCO_2 algorithm within the SOM-defined
693 sub-regions. The model used simple empirical relationships between carbonate chemistry (DIC
694 and Alk) and satellite data (SST and *Chl*). Surface-water pCO_2 was calculated from the
695 empirically-predicted DIC and Alk. This directly incorporated the inherent nonlinearities of the
696 carbonate system, in a completely mechanistic manner.
697

Appendix A – Additional Sources of Surface Ocean pCO_2 not included in the SOCAT Data

A.1 South Atlantic Bight

Underway surface ocean pCO_2 data from the SAB were collected by Dr. Wei-Jun Cai (a co-author in this study) and co-workers at the Department of Marine Sciences, University of Georgia. A total of 65,454 underway surface ocean pCO_2 records were processed for this study from six cruises along the SAB continental shelf: 5–16 January 2005, 19–30 March 2005, 27 July to 5 August 2005, 7–17 October 2005, 16–21 December 2005, and 17–27 May 2006. The SOCAT data set includes the 2005 cruises but not those undertaken in 2006, which were added to our analysis to include all cruises. In all of the sampling cruises except for the one in December 2005, the research vessel transected the whole SAB from coastline to about 500-m water depth. The survey focused on 5 cross-shelf transects that are named E-, D-, C-, B-, and A-transect, respectively from north to south. In December 2005, the ship transected the whole SAB, but did not cover D- and B-transects and did not go beyond the 200 m isobaths due to limited ship time. Surface water and atmospheric xCO_2 were measured underway during all cruises. Sea surface temperature (SST) and salinity were recorded continuously with an onboard SeaBird flow through thermosalinograph. Sea level pressure was recorded using an onboard R.M. Young barometric pressure sensor. Surface water xCO_2 was measured using a LI-COR 7000 infrared gas analyzer coupled to a gas-water equilibrator. Details of the methodology and accuracy of instruments used are given in *Jiang et al.* [2008]. Fig. A-1 shows the data distribution map.

A.2 Gulf of Maine

Underway surface ocean pCO_2 data from monthly cruises in the southern Gulf of Maine were obtained from the University of New Hampshire (UNH) and integrated with the SOCAT data base. Underway data are measured continuously from pumped surface water for physical,

chemical, biological and bio-optical properties. The data used in this study consisted of 309,665 surface observations spanning the period of 2004-2010. These data originate from the UNH Coastal Ocean Observing Center's Coastal Carbon Group, which is an interdisciplinary research team within UNH-EOS engaged in efforts to observe and model how the Earth's pool of carbon moves between the land, ocean, and atmosphere with a particular focus on how this carbon cycling occurs in coastal regions, such as the Gulf of Maine. Dr. Joe Salisbury, a co-author in this study, is a member of the UNH Coastal Carbon Group. The methodology and instrumentation details are given in *Vandermark et al*. [2011]. The precision of the fCO_2 measurements was ±3 μatm. Fig. A-2 shows the data distribution map. All underway cruise tracks are in the GoM, except for a single cruise track from Woods Hole to New York City.

A. 3 Scotian Shelf

Underway (UW) surface ocean pCO_2 data from transects across the Scotian Shelf, and high frequency pCO_2, SST, SSS and calibrated fluorometer Chl data from the CARIOCA buoy were obtained from Dalhousie University [*Shadwick et al*., 2010; *Shadwick et al*., 2011]. These data were used to evaluate the algorithm performance on the Scotian Shelf. Hourly, autonomous observations of surface water pCO_2 (μatm), chlorophyll-*a* fluorescence (F_{Chl}), and SST, were made using a CARIOCA buoy moored roughly 30 km offshore from Halifax, at 44.3° N and 63.3°W, between April 2007 and June 2008. Hourly CARIOCA data were uploaded and transmitted daily via the ARGOS satellite system. The pCO_2 measurements were made by an automated spectrophotometric technique. A Sea-Bird (SBE 41) conductivity and temperature sensor was used to measure temperature (◦C) and to determine salinity; chlorophyll-*a* fluorescence (μg l^{-1}) was determined by a WET Labs miniature fluorometer (WETstar). Non-

745 photochemical effects that are related to the intensity of the incoming solar radiation may
746 decrease F_{Chl} up to 80% during the day. This effect can be avoided by using night-time data
747 which, to a large extent, are free of the effects of non-photochemical quenching, for fluorometer
748 calibration. Night-time data were taken as a mean F_{Chl} between 03:00 and 06:00 UTC (or 11:00
749 and 02:00 LT); data points were temporally interpolated to match discrete chlorophyll-*a*
750 measurements (Chl-*a* in mg m^{-3}) from monthly or twice monthly occupations at the mooring site.
751 Chl-*a* concentration was determined fluorometrically in a Turner Designs fluorometer using the
752 acid ratio technique for seawater samples collected at 3, 5, or 10m depth. A linear regression (r^2
753 = 0.76, N=29, $p < 0.001$) was used to determine the relationship between the F_{Chl} and Chl-*a*, and
754 applied to the CARIOCA fluorescence-derived Chl-*a* time-series (Chl_F in mg m^{-3}). *Shadwick et*
755 *al*. [2010] performed a validation of satellite monthly chlorophyll data by regressing it against
756 the (night-time calibrated), monthly mean, CARIOCA Chl_F time series, (r^2 =0.68, N=14, p
757 <0.002).
758 Measurements of pCO_2 UW were made by a continuous flow equilibration system in:
759 October 2006, April, August, and October 2007, and April and October, 2008 on board the
760 *CCGS Hudson*. The UW measurements (see distribution map in Fig. 7a) were obtained on
761 monitoring cruises on the Scotian Shelf (see *Shadwick et al*., 2011 for details of the field
762 program). Measurements of pCO_2 UW were made by a non-dispersive, infrared spectrometer
763 (LiCor, LI-7000). The system was located in the aft-laboratory of the ship and the intake depth
764 was approximately 3m below the water surface. Measurements were made every minute and
765 used to compute hourly averages. The system was calibrated daily with both a CO_2-free
766 reference gas (N_2) and a CO_2 calibration gas (328.99 ppm) provided by the US National Oceanic

767 and Atmospheric Administration (NOAA). The data were corrected to in-situ water temperature
768 and to 100% humidity and had an associated uncertainty of less than 1μatm.
769
770
771
772 ***Acknowledgements***
773 We wish to acknowledge the NASA Ocean Biology and Biogeochemistry program for
774 providing funds for this project. We also want to acknowledge Mr. Daniel Tomaso for providing
775 the compiled climatologic data sets for sea surface salinity and mixed layer depth, and
776 Environment Canada for making available the wind data from Sable Island.
777
778

References

Alberts, J. J., and M. Takacs (1999), Importance of humic substances for carbon and nitrogen transport into southeastern United States estuaries, *Organic Geochemistry*, *30*(6), 385-395.

Atlas, R., R. N. Hoffman, J. Ardizzone, S. M. Leidner, J. C. Jusem, D. K. Smith, D. Gombos, (2011), A cross-calibrated, multiplatform ocean surface wind velocity product for meteorological and oceanographic applications. *Bull. Amer. Meteor. Soc*., *92*, 157-174. Doi: 10.1175/2010BAMS2946.1

Borges, A. V. (2005), Do we have enough pieces of the jigsaw to integrate CO_2 fluxes in the coastal ocean?, *Estuaries*, *28*(1), 3-27.

Borges, A. V., B. Delille, and M. Frankignoulle (2005), Budgeting sinks and sources of CO_2 in the coastal ocean: Diversity of ecosystems counts, *Geophysical Research Letters*, *32*(14), doi:10.1029/2005GL023053.

Borges, A. V., B. Tilbrook, N. Metzl, A. Lenton, and B. Delille (2008), Inter-annual variability of the carbon dioxide oceanic sink south of Tasmania, *Biogeosciences*, *5*(1), 141-155.

Cai, W.-J., Wang, Y., Hodson, R.E. (1998). Acid-base properties of dissolved organic matter in the estuarine waters of Georgia, *Geochimica et Cosmochimica Acta, 62*, 473-483.

Cai, W. J., M. H. Dai, and Y. C. Wang (2006), Air-sea exchange of carbon dioxide in ocean margins: A province-based synthesis, *Geophysical Research Letters*, *33*(12), doi:10.1029/2006GL026219.

Cai, W. J., X. P. Hu, W. J. Huang, L. Q. Jiang, Y. C. Wang, T. H. Peng, and X. Zhang (2010), Alkalinity distribution in the western North Atlantic Ocean margins, *Journal of Geophysical Research-Oceans*, *115,* doi:10.1029/2009JC005482.

Cai, W. J. (2011), Estuarine and Coastal Ocean Carbon Paradox: CO_2 Sinks or Sites of Terrestrial Carbon Incineration?, in *Annual Review of Marine Science, Vol 3*, edited by C. A. Carlson and S. J. Giovannoni, pp. 123-145.

Carr, M. E., et al. (2006), A comparison of global estimates of marine primary production from ocean color, *Deep-Sea Res. Part II-Topical Studies in Oceanography*, *53*(5-7), 741-770.

Chapman, D. C., and R. C. Beardsley (1989), On The Origin of Shelf Water in The Middle Atlantic Bight, *Journal of Physical Oceanography*, *19*(3), 384-391.

Craig, S. E., Thomas, H., Jones, C. T., Li, W. K. W., Greenan, B. J. W., Shadwick, E. H., and Burt, W. J. (2013), Temperature and phytoplankton cell size regulate carbon uptake and carbon overconsumption in the ocean - *Biogeosciences Discussion*, *10*, 11255-11282, doi:10.5194/bgd-10-11255-2013.

DeGrandpre, M. D., G. J. Olbu, C. M. Beatty, and T. R. Hammar (2002), Air-sea CO_2 fluxes on the US Middle Atlantic Bight, *Deep-Sea Res. Part II-Topical Studies in Oceanography*, *49*(20), 4355-4367.

Dickson, A. G. (1990), Standard potential of the reaction – AGCL(S)+1/2H-2(G)=AG(S)+HCL(aq) and the standard acidity constant of the ion $HSO4^-$ in synthetic sea-water from 273.15 ^oK to 318.15 ^oK, *Journal of Chemical Thermodynamics*, *22*(2), 113-127.

Dickson, A. G., and F. J. Millero (1987), A comparison of the equilibrium constants for the dissociation of carbonic acid in seawater media, *Deep-Sea Res. Part A – Oceanographic Research Papers*, *34*(10), 1733-1743.

Fox, M. F., D. R. Kester, and J. A. Yoder (2005), Spatial and temporal distributions of surface temperature and chlorophyll in the Gulf of Maine during 1998 using SeaWiFS and AVHRR imager, *Marine Chemistry*, *97*(1-2), 104-123.

824 Frankignoulle, M., and A. V. Borges (2001), European continental shelf as a significant sink for
825 atmospheric carbon dioxide, *Global Biogeochemical Cycles*, *15*(3), 569-576.
826 Friedrich, T., and A. Oschlies (2009), Neural network-based estimates of North Atlantic surface
827 pCO_2 from satellite data: A methodological study, *J. Geophys. Res.-Oceans*, *114,* C03020, doi:
828 10.1029/2007JC004646.
829 Burke Hales, Wei-Jun Cai, B. Greg Mitchell, Christopher L. Sabine, and Oscar Schofield [eds.],
830 2008: *North American Continental Margins: A Synthesis and Planning Workshop*. Report of the
831 North American Continental Margins Working Group for the U.S. Carbon Cycle Scientific
832 Steering Group and Interagency Working Group. U.S. Carbon Cycle Science Program,
833 Washington, DC, 110 pp.
834 Hales, B., P. G. Strutton, M. Saraceno, R. Letelier, T. Takahashi, R. A. Feely, C. L. Sabine, and
835 F. Chavez (2012), Satellite-based prediction of pCO_2 in coastal waters of the eastern North
836 Pacific, *Progress in Oceanography*, *103*, 1-15, doi:10.1016/j.pocean.2012.03.001.
837 GLOBALVIEW-CO2 (2011), Cooperative Atmospheric Data Integration Project – Carbon
838 Dioxide. CD-ROM, NOAA ESRL, Boulder, Colorado [Also available on Internet via
839 anonymous FTP to ftp.cmdl.noaa.gov, Path: ccg/co2/GLOBALVIEW].
840 Ho, D. T., R. Wanninkhof, P. Schlosser, D. S. Ullman, D. Hebert, and K. F. Sullivan (2011),
841 Toward a universal relationship between wind speed and gas exchange: Gas transfer velocities
842 measured with $^3He/SF_6$ during the Southern Ocean gas exchange experiment, *J. of Geophys.*
843 *Res.*, 116, C00F04, doi:10.1029/2010JC006854.
844 Hofmann, E., et al. (2008), Eastern US Continental Shelf Carbon Budget Integrating Models,
845 Data Assimilation, and Analysis, *Oceanography*, *21*(1), 86-104.
846 Hofmann, E. E., et al. (2011), Modeling the Dynamics of Continental Shelf Carbon, in *Annual*
847 *Review of Marine Science, Vol 3*, edited by C. A. Carlson and S. J. Giovannoni, pp. 93-122.
848 Jiang, L.-Q., W.-J. Cai, R. Wanninkhof, Y. Wang, and H. Lüger (2008), Air-sea CO_2 fluxes on
849 the U.S. South Atlantic Bight: Spatial and seasonal variability, *J. Geophys. Res., 113*, C07019,
850 doi:10.1029/2007JC004366.
851 Jiang, L.-Q., Cai, W.-J., Wang, Y., and Bauer, J. E. (2013), Influence of terrestrial inputs on
852 continental shelf carbon dioxide, *Biogeosciences*, *10*, 839-849, doi:10.5194/bg-10-839-2013.
853 Joyce, T. M., J. K. B. Bishop, and O. B. Brown (1992), Observations of offshore shelf-water
854 transport induced by a warm-core ring, *Deep-Sea Res. I – Oceanographic Research Papers*,
855 *39*(1A), S97-S113.
856 Kalnay, E., M. Kanamitsu, R. Kistler, W. Collins, D. Deaven, L. Gandin, M. Iredell, S. Saha, G.
857 White, J. Woollen, Y. Zhu, A. Leetma, B. Reynolds, M. Chelliah, W. Ebisuzaki, W. Higgins, J.
858 Janowiak, K. C. Mo, R. Ropelewski, J. Wang, R. Jenne, and D. Joseph (1996), The
859 NCEP/NCAAR 40-year Reanalysis Project, Bull. Amer. Met. Soc., March 1996.
860 Laruelle, G. G., H. H. Durr, C. P. Slomp, and A. V. Borges (2010), Evaluation of sinks and
861 sources of CO_2 in the global coastal ocean using a spatially-explicit typology of estuaries and
862 continental shelves, *Geophysical Research Letters*, *37,* doi:10.1029/2010GL043691.
863 Le Quéré, C., T. Takahashi, E. T. Buitenhuis, C. Rodenbeck, and S. C. Sutherland (2010),
864 Impact of climate change and variability on the global oceanic sink of CO_2, *Global*
865 *Biogeochemical Cycles*, *24*.
866 Lee, K., R. Wanninkhof, R. A. Feely, F. J. Millero, and T. H. Peng (2000), Global relationships
867 of total inorganic carbon with temperature and nitrate in surface seawater, *Global*
868 *Biogeochemical Cycles*, *14*(3), 979-994.

Lee, K., L. T. Tong, F. J. Millero, C. L. Sabine, A. G. Dickson, C. Goyet, G. H. Park, R. Wanninkhof, R. A. Feely, and R. M. Key (2006), Global relationships of total alkalinity with salinity and temperature in surface waters of the world's oceans, *Geophysical Research Letters*, *33*(19), doi:10.1029/2006GL027207.

Lee, Z. P., and K. L. Carder (2004), Absorption spectrum of phytoplankton pigments derived from hyperspectral remote-sensing reflectance, *Remote Sensing of Environment*, *89*(3), 361-368.

Lee, Z. P., R. Arnone, C. M. Hu, P. J. Werdell, and B. Lubac (2010), Uncertainties of optical parameters and their propagations in an analytical ocean color inversion algorithm, *Applied Optics*, *49*(3), 369-381.

Lefèvre, N., A. J. Watson, and A. R. Watson (2005), A comparison of multiple regression and neural network techniques for mapping in situ pCO_2 data, *Tellus Series B-Chemical and Physical Meteorology*, *57*(5), 375-384.

Lohrenz, S. E., and W. J. Cai (2006), Satellite ocean color assessment of air-sea fluxes of CO_2 in a river-dominated coastal margin, *Geophysical Research Letters*, *33*(1), doi:10.1029/2005GL023942.

Loisel, H., E. Bosc, D. Stramski, K. Oubelkheir, and P. Y. Deschamps (2001), Seasonal variability of the backscattering coefficient in the Mediterranean Sea based on Satellite SeaWiFS imagery, *Geophysical Research Letters*, *28*(22), 4203-4206.

O'Reilly, J. E., and C. Zetlin (1998), Seasonal, Horizontal, and Vertical Distribution of Phytoplankton Chlorophyll a in the Northeast U.S. Continental Shelf Ecosystem, in *Fishery Bulletin*, edited, p. 120, NOAA.

Pfeil, B., Olsen, A., Bakker, D. C. E., Hankin, S., Koyuk, H., Kozyr, A., Malczyk, J., Manke, A., Metzl, N., Sabine, C. L., Akl, J., Alin, S. R., Bellerby, R. G. J., Borges, A., Boutin, J., Brown, P. J., Cai, W.-J., Chavez, F. P., Chen, A., Cosca, C., Fassbender, A. J., Feely, R. A., González-Dávila, M., Goyet, C., Hardman-Mountford, N., Heinze, C., Hood, M., Hoppema, M., Hunt, C. W., Hydes, D., Ishii, M., Johannessen, T., Jones, S. D., Key, R. M., Körtzinger, A., Landschützer, P., Lauvset, S. K., Lefèvre, N., Lenton, A., Lourantou, A., Merlivat, L., Midorikawa, T., Mintrop, L., Miyazaki, C., Murata, A., Nakadate, A., Nakano, Y., Nakaoka, S., Nojiri, Y., Omar, A. M., Padin, X. A., Park, G.-H., Paterson, K., Perez, F. F., Pierrot, D., Poisson, A., Ríos, A. F., Santana-Casiano, J. M., Salisbury, J., Sarma, V. V. S. S., Schlitzer, R., Schneider, B., Schuster, U., Sieger, R., Skjelvan, I., Steinhoff, T., Suzuki, T., Takahashi, T., Tedesco, K., Telszewski, M., Thomas, H., Tilbrook, B., Tjiputra, J., Vandemark, D., Veness, T., Wanninkhof, R., Watson, A. J., Weiss, R., Wong, C. S., and Yoshikawa-Inoue, H.: A uniform, quality controlled Surface Ocean CO_2 Atlas (SOCAT), *Earth Syst. Sci. Data Discuss*., *5*, 735-780, doi:10.5194/essdd-5-735-2012, 2012.

Rossby, T. (1987), On the energetics of the Gulf Stream at 73W, *Journal of Marine Research*, *45*(1), 59-82.

Salisbury, J. E., D. Vandemark, C. W. Hunt, J. W. Campbell, W. R. McGillis, and W. H. McDowell (2008), Seasonal observations of surface waters in two Gulf of Maine estuary-plume systems: Relationships between watershed attributes, optical measurements and surface pCO_2, *Estuarine Coastal and Shelf Science*, *77*(2), 245-252.

Shadwick, E. H., H. Thomas, A. Comeau, S. E. Craig, C. W. Hunt, and J. E. Salisbury (2010), Air-Sea CO_2 fluxes on the Scotian Shelf: seasonal to multi-annual variability, *Biogeosciences*, *7*(11), 3851-3867.

913 Shadwick, E. H., H. Thomas, K. Azetsu-Scott, B. J. W. Greenan, E. Head, and E. Horne (2011),
914 Seasonal variability of dissolved inorganic carbon and surface water pCO_2 in the Scotian Shelf
915 region of the Northwestern Atlantic, *Marine Chemistry*, *124*(1-4), 23-37.
916 Shearman, R. K., and S. J. Lentz (2004), Observations of tidal variability on the New England
917 shelf, *Journal of Geophysical Research-Oceans*, *109*(C6), doi:10.1029/2003JC001972.
918 Smith, W. H. F, and P. Wessel (1990), Gridding with continuous curvature splines in tension,
919 *Geophysics*, 55, 293−305.
920 Signorini, S. R., and C. R. McClain (2007), Large-scale forcing impact on biomass variability in
921 the South Atlantic Bight, *Geophys. Res. Lett.*, *34*(21), doi:10.1029/2007GL031121.
922 Stramski, D., R. A. Reynolds, M. Kahru, and B. G. Mitchell (1999), Estimation of particulate
923 organic carbon in the ocean from satellite remote sensing, *Science*, *285*(5425), 239-242.
924 Takahashi, T., et al. (2002), Global sea-air CO_2 flux based on climatological surface ocean pCO_2,
925 and seasonal biological and temperature effects, *Deep-Sea Research Part II-Topical Studies In*
926 *Oceanography*, *49*(9-10), 1601-1622.
927 Takahashi T., Sutherland S.C., Wanninkhof R., Sweeney C., Feely R.A., et al. (2009),
928 Climatological mean and decadal change in surface ocean pCO_2, and net sea-air CO_2 flux over
929 the global oceans. *Deep-Sea Res.* II, 56:554–77.
930 Telszewski, M., et al. (2009), Estimating the monthly pCO_2 distribution in the North Atlantic
931 using a self-organizing neural network, *Biogeosciences*, *6*(8), 1405-1421.
932 Thomas, A. C., D. W. Townsend, and R. Weatherbee (2003), Satellite-measured phytoplankton
933 variability in the Gulf of Maine, *Continental Shelf Research*, *23*(10), 971-989.
934 Thomas, H., and A. V. Borges (2012), Biogeochemistry of coastal seas and continental shelves –
935 Including biogeochemistry during the International Polar Year, *Estuarine Coastal and Shelf*
936 *Science*, *100*, 1-2.
937 Thomas, H., S. E. Craig, B. J. W. Greenan, W. Burt, G. J. Herndl, S. Higginson, L. Salt, E. H.
938 Shadwick, and J. Urrego-Blanco (2012), Direct observations of diel biological CO_2 fixation on
939 the Scotian Shelf, northwestern Atlantic Ocean, *Biogeosciences*, *9*, 2301-2309, doi:10.5194/bg-
940 9-2301-2012.
941 Thomas, H., L. S. Schiettecatte, K. Suykens, Y. J. M. Kone, E. H. Shadwick, A. E. F. Prowe, Y.
942 Bozec, H. J. W. de Baar, and A. V. Borges (2009), Enhanced ocean carbon storage from
943 anaerobic alkalinity generation in coastal sediments, *Biogeosciences*, *6*(2), 267-274.
944 Thomas, H. (2004), Enhanced open ocean storage of CO_2 from shelf sea pumping, *Science*,
945 *304(1005)*, doi:10.1126/science.1095491.
946 Uppstrom, L. (1974), Boron/chlorinity ratio of deep-sea water from Pacific Ocean, *Deep-Sea*
947 *Res, 21(2),* 161-162, doi:10.1016/0011-7471(74)90074-6.
948 Vandemark, D., J. E. Salisbury, C. W. Hunt, S. M. Shellito, J. D. Irish, W. R. McGillis, C. L.
949 Sabine, and S. M. Maenner (2011), Temporal and spatial dynamics of CO_2 air-sea flux in the
950 Gulf of Maine, *Journal of Geophysical Research-Oceans*, *116,* doi:10.1029/2010JC006408.
951 Verity, P. G., J. E. Bauer, C. N. Flagg, D. J. DeMaster, and D. J. Repeta (2002), The Ocean
952 Margins Program: an interdisciplinary study of carbon sources, transformations, and sinks in a
953 temperate continental margin system, *Deep-Sea Research Part II-Topical Studies in*
954 *Oceanography*, *49*(20), 4273-4295.
955 Wang, Z. A., R. Wanninkhof, W. J. Cai, R. H. Byrne, X. Hu, T. H. Peng, and W. J. Huang
956 (2013), The marine inorganic carbon system along the Gulf of Mexico and Atlantic Coasts of the
957 United States: Insights from a transregional coastal carbon study. Limnol. Oceanogr. *58***,** 325-
958 342.

Wang, Z. A., W. J. Cai, Y. C. Wang, and H. W. Ji (2005), The southeastern continental shelf of the United States as an atmospheric CO_2 source and an exporter of inorganic carbon to the ocean, *Continental Shelf Research*, *25*(16), 1917-1941.
Wang, Z. H. A., and W. J. Cai (2004), Carbon dioxide degassing and inorganic carbon export from a marsh-dominated estuary (the Duplin River): A marsh CO_2 pump, *Limnology and Oceanography*, *49*(2), 341-354.
Wanninkhof, R. (1992), Relationship Between Wind-Speed And Gas-Exchange Over The Ocean, *J. Geophys. Res.-Oceans*, *97*(C5), 7373-7382.
Wanninkhof, R., A. Olsen, and J. Trinanes (2007), Air-sea CO_2 fluxes in the caribbean sea from 2002-2004, *Journal of Marine Systems*, *66*(1-4), 272-284.
Wanninkhof, R., W. E. Asher, D. T. Ho, C. Sweeney, and W. McGillis (2009), Advances in quantifying air-sea gas exchange and environmental forcing, *Annu. Rev. Mar. Sci.*, *1*, 213-244.
Wessel, P., and W. H. F. Smith (1991), Free software helps map and display data, Eos Trans. AGU, 72, 441, doi:10.1029/90EO00319.
Whitney, M. M. (2010), A study on river discharge and salinity variability in the Middle Atlantic Bight and Long Island Sound, *Continental Shelf Research*, *30*(3-4), 305-318.

977
978

Table 1. Coefficients and statistical data for pCO_2 algorithm (Equation 1). The multiple regression coefficients and their corresponding standard errors were obtained using the MatLab function 'regstats' with *t* statistics.

Means and Coefficients	SAB	MAB	GB+NS	GoM	SS
T_o (^oC)	23.21	15.27	11.27	10.29	7.34
S_o (psu)	35.38	31.64	32.19	31.41	30.58
γ (days)	123	218	359	343	27
Chl_o (mg m^{-3})	1.09	1.54	1.62	2.94	1.24
a (μatm)	378.69 ±1.76	360.07 ±1.40	370.66 ±1.84	373.06 ±1.38	351.43 ±0.90
b (μatm)	24.00 ±2.05	7.03 ±4.82	37.05 ±2.63	39.43 ±1.68	69.31 ±2.39
c (μatm $^oC^{-1}$)	12.23 ±0.36	5.20 ±0.47	6.88 ±0.40	1.65 ±0.24	8.77 ±0.26
d (μatm psu^{-1})	-22.49 ±1.71	1.11 ±0.61	-10.95 ±2.33	-1.34 ±0.83	1.44 ±0.86
e (μatm/$\log_{10}(Chl)$)	30.25 ±5.87	-14.99 ±5.51	10.05 ±7.67	-20.65 ±3.83	-100.32 ±4.66
r^2	0.82	0.55	0.60	0.42	0.74
RMSE (μatm)	26.7	36.9	32.2	34.6	22.4
N	356	997	356	847	684

979
980

981

Table 2. Sea-air CO_2 flux for reference year 2004 from binned data, algorithm for year 2004, and previous studies (literature). Uncertainties (ϵ) for the estimates from the data were obtained as $\epsilon = \mathrm{STD}/\sqrt{N}$, where STD is the standard deviation and *N* the number of data points. Uncertainties for the sea-air CO_2 flux estimates from the algorithm were based on the standard deviation of all monthly estimates for the period 2003-2010. Both specific (mol CO_2 m^{-2} yr^{-1}) and total (Tg C yr^{-1}) sea-air fluxes are shown for each region and total for the whole coast. Two gas transfer coefficients were used, the polynomial equation of *Wanninkhof et al.* [2009] (k^1_{660}) and the quadratic dependence version of *Ho et al.* [2011] (k^2_{660}) adjusted for steady winds using the nonlinearity coefficients C_2 and C_3.

Region	**Area** 10^{10} **m²**	**Data** mol CO_2 m^{-2} yr^{-1} Tg C yr^{-1}		**Algorithm** mol CO_2 m^{-2} yr^{-1} Tg C yr^{-1}		**Literature** mol CO_2 m^{-2} yr^{-1} Tg C yr^{-1}
		k^1_{660}	k^2_{660}	k^1_{660}	k^2_{660}	
SS	12.82	-1.10 ± 0.25	-1.21 ± 0.27	-0.39 ± 0.34	-0.42 ± 0.36	+1.42 ± 0.28 (*d*)
		-1.69 ± 0.39	-1.87 ± 0.42	-0.56 ± 0.50	-0.60 ± 0.53	+2.19 ± 0.43
GoM	12.77	+0.11 ± 0.21	+0.04 ± 0.22	+0.01 ± 0.08	+0.01± 0.08	+0.38 ± 0.26 (c)
		+0.17 ± 0.32	+0.06 ± 0.34	+0.02 ± 0.12	+0.02 ± 0.12	+0.58 ± 0.40
GB+NS	5.83	-0.65 ± 0.20	-0.71 ± 0.22	-1.27 ± 0.23	-1.37 ± 0.24	-
		-0.46 ± 0.14	-0.50 ± 0.15	-0.79 ± 0.16	-0.86 ± 0.16	-
MAB	9.31	-0.95 ± 0.24	-1.07 ± 0.27	-1.58 ± 0.19	-1.78 ± 0.19	-1.1 ± 0.7
		-1.06 ± 0.27	-1.12 ± 0.30	-1.63 ± 0.21	-1.83 ± 0.22	-1.0 ± 0.6 (*a*)
SAB	10.20	-0.79 ± 0.26	-0.68 ± 0.24	-0.61 ± 0.17	-0.67± 0.16	-0.48 ± 0.21(*b*)
		-0.97 ± 0.31	-0.83 ± 0.29	-0.67 ± 0.20	-0.74 ± 0.20	-0.59 ± 0.26
Total	50.63	-4.01 ± 0.30	-4.26 ± 0.31	-3.63 ± 0.24	-4.01 ± 0.25	-

(*a*) *DeGrandpre* [2002]; (*b*) *Jiang et al.* [2008]; (*c*) *Vandemark et al*. [2011] is 5-year mean (2004-2208) but ranging from +0.71 (2005) to -0.11 (2007) mol m^{-2} yr^{-1}; (*d*) *Shadwick et al*. [2011]. Values for (b), (c), and (d) were converted from specific to total flux, or mol CO_2 m^{-2} yr^{-1} to Tg C yr^{-1} ($\times 12 \times \mathrm{area} \times 10^{-12}$). $k^1_{660} = 3 + 0.1U_{10} + 0.064C_2U^2_{10} + 0.011C_3U^3_{10}$ and $k^2_{660} = 0.262C_2U^2_{10}$

982

983

Table 3. Sea-air CO_2 flux derived from the regional algorithms for 2003-2010. The flux is given in two different units for each year (mol CO_2 m^{-2} yr^{-1}/Tg C yr^{-1}), and in Tg C yr^{-1} for the overall 8-year mean and whole coast sum. The flux was calculated using the gas transfer equation of *Ho et al*. [2011].

Year	SAB	MAB	GoM	GB+NS	SS	Sum
2003	-0.78/-0.90	-2.18/-2.43	+0.002/+0.009	-1.72/-1.20	-0.33/-0.55	-5.07
2004	-0.75/-0.88	-2.08/-2.31	+0.107/+0.166	-1.72/-1.20	-0.27/-0.39	-4.61
2005	-0.95/-1.12	-1.92/-2.13	+0.068/+0.108	-1.49/-1.04	+0.18/+0.15	-4.03
2006	-0.74/-0.88	-1.56/-1.73	-0.052/-0.074	-1.05/-0.73	-0.01/-0.02	-3.43
2007	-0.43/-0.51	-1.76/-1.95	-0.129/-0.191	-1.71/-1.20	-1.01/-1.55	-5.40
2008	-0.78/-0.93	-1.72/-1.91	-0.045/-0.062	-1.21/-0.85	-0.55/-0.77	-4.52
2009	-0.66/-0.76	-1.90/-2.11	-0.024/-0.028	-1.32/-0.92	-0.72/-1.14	-4.96
2010	-0.91/-1.08	-2.16/-2.41	+0.079/+0.126	-1.21/-0.85	-0.18/-0.40	-4.62
Mean	-0.89±0.18	-2.12±0.24	+0.007±0.112	-1.00±0.18	-0.58±0.52	-4.58

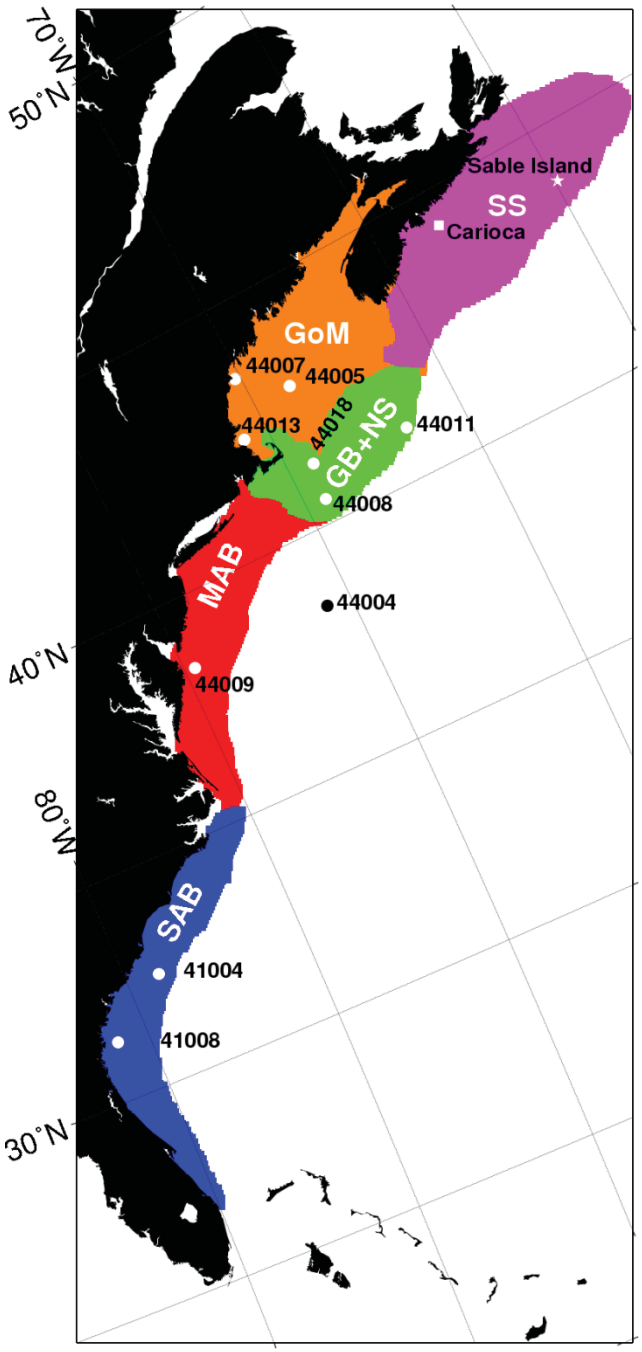

Fig. 1. Regional domains for analysis adapted from *Hofmann et al*. [2008] and *Hofmann et al* [2011]. The white circles show the locations of the NDBC buoys within each regional domain. The white star shows the location of the Sable Island meteorological station and the white square the location of the Carioca buoy.

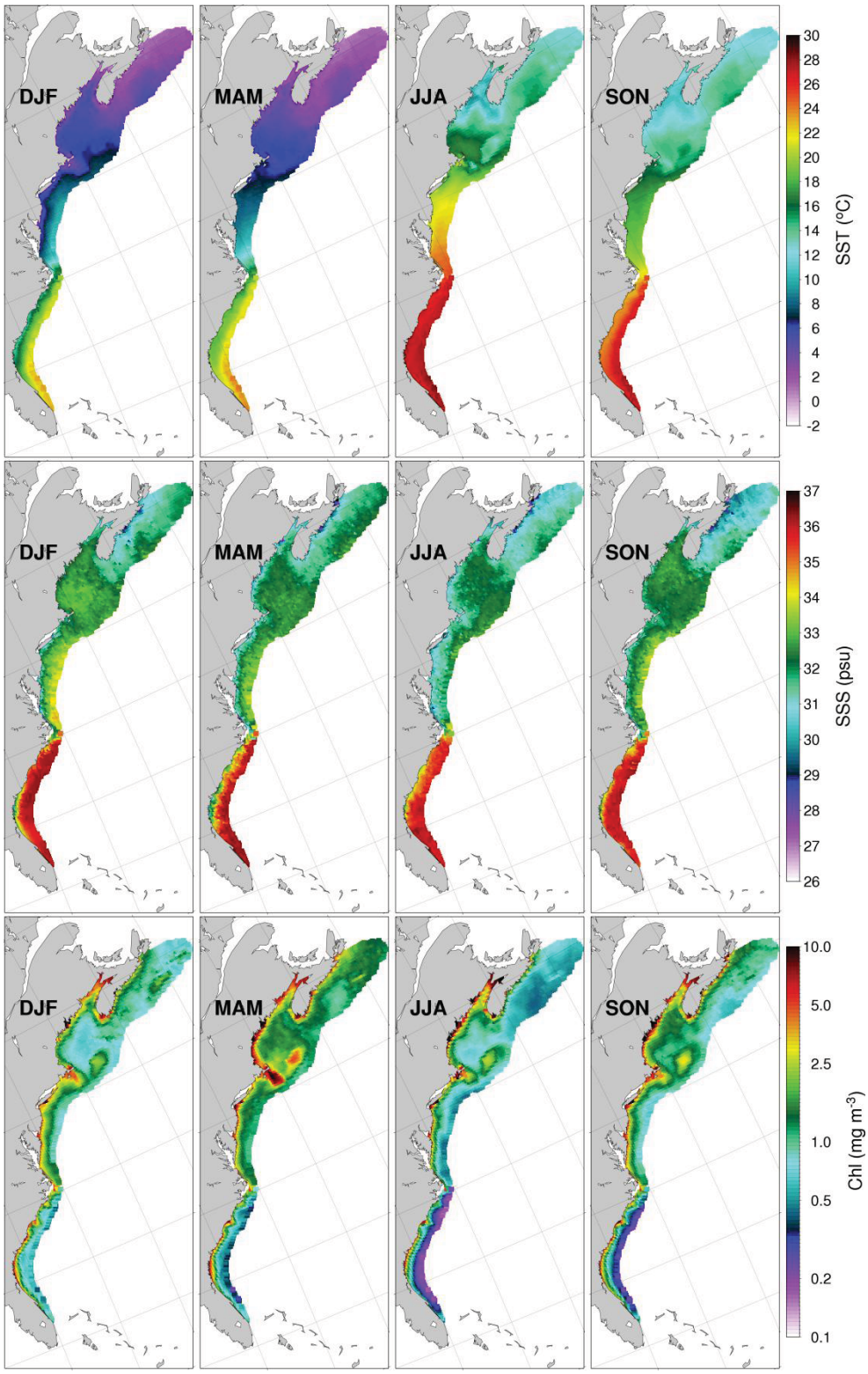

Fig. 2. Seasonal climatology maps of SST, SSS, and *Chl*. Upper row: SST composites from MODIS Aqua; middle row: SSS composites from World Ocean Data 2009; bottom row: *Chl* composites from MODIS Aqua. Refer to the methods section (3.0) for details. The MODIS SST and *Chl* seasonal climatologies are based on the period 2002-2011. The seasons are defined as Dec-Jan-Feb (DJF), Mar-Apr-May (MAM), Jun-Jul-Aug (JJA), and Sep-Oct-Nov (SON).

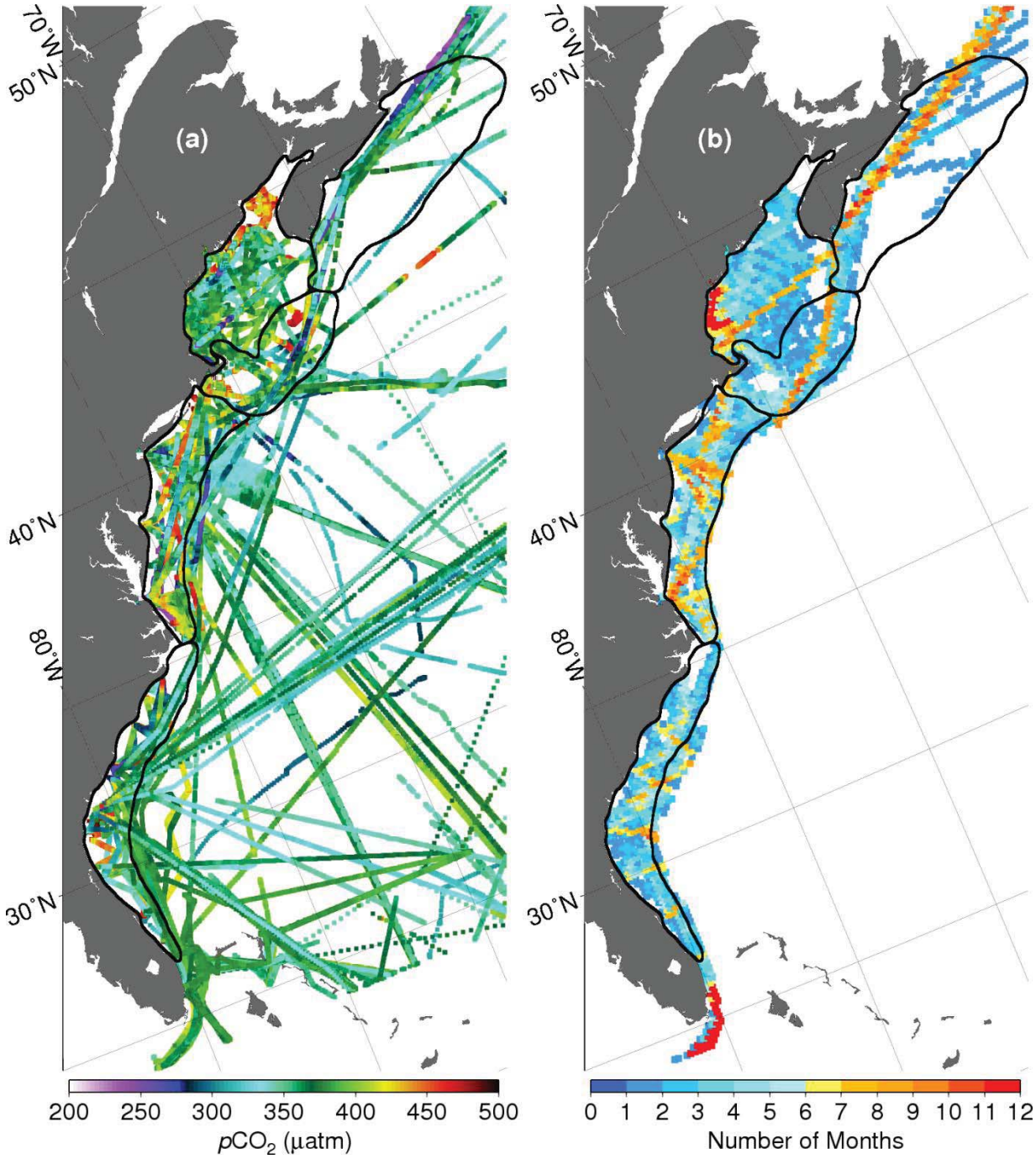

Fig. 3. Color-coded SOCAT surface ocean pCO_2 cruise tracks (a) and corresponding coastal binned data (b) with associated color-coded temporal coverage in months. The highest temporal coverage corresponds to the most travelled routes (in orange to red), i.e., most frequent destination ports (Boston, New York, Norfolk, Miami) used by the Volunteering Observing Ships. The SOCAT data set also includes transects occupied by research vessels. The SS, GoM, GB+NS, MAB and SAB regional boundaries are overlaid as black lines.

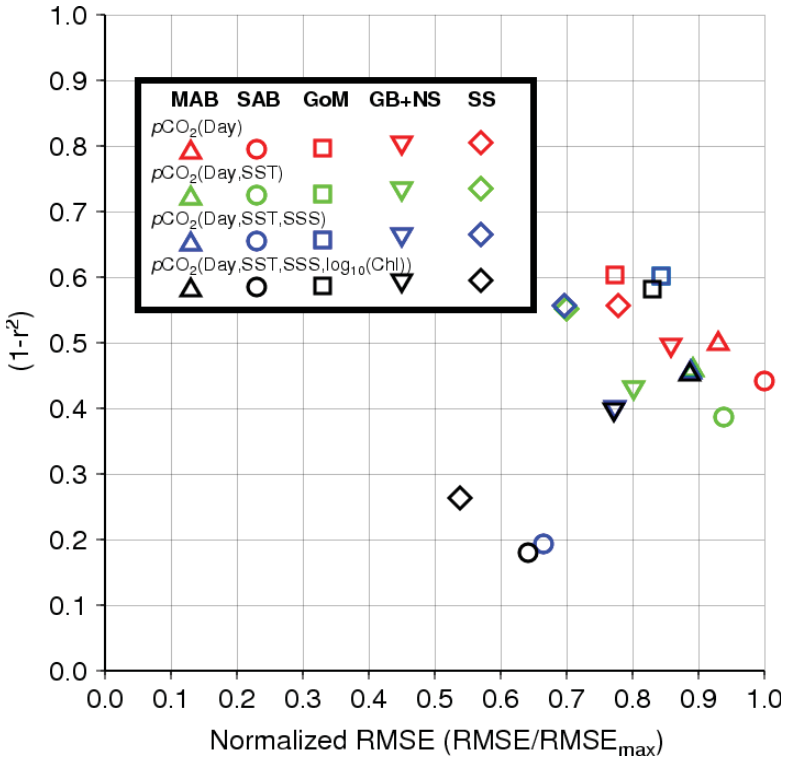

Fig. 4. Plot of goodness-of-fit statistics for all regional MLRs with incremental addition of corresponding proxy parameters. The *x*-axis shows the RMSE normalized by the maximum attained value among all MLRs, while the *y*-axis shows (1-r^2). Thus a perfect match between data and MR values would be centered at the origin (0, 0).

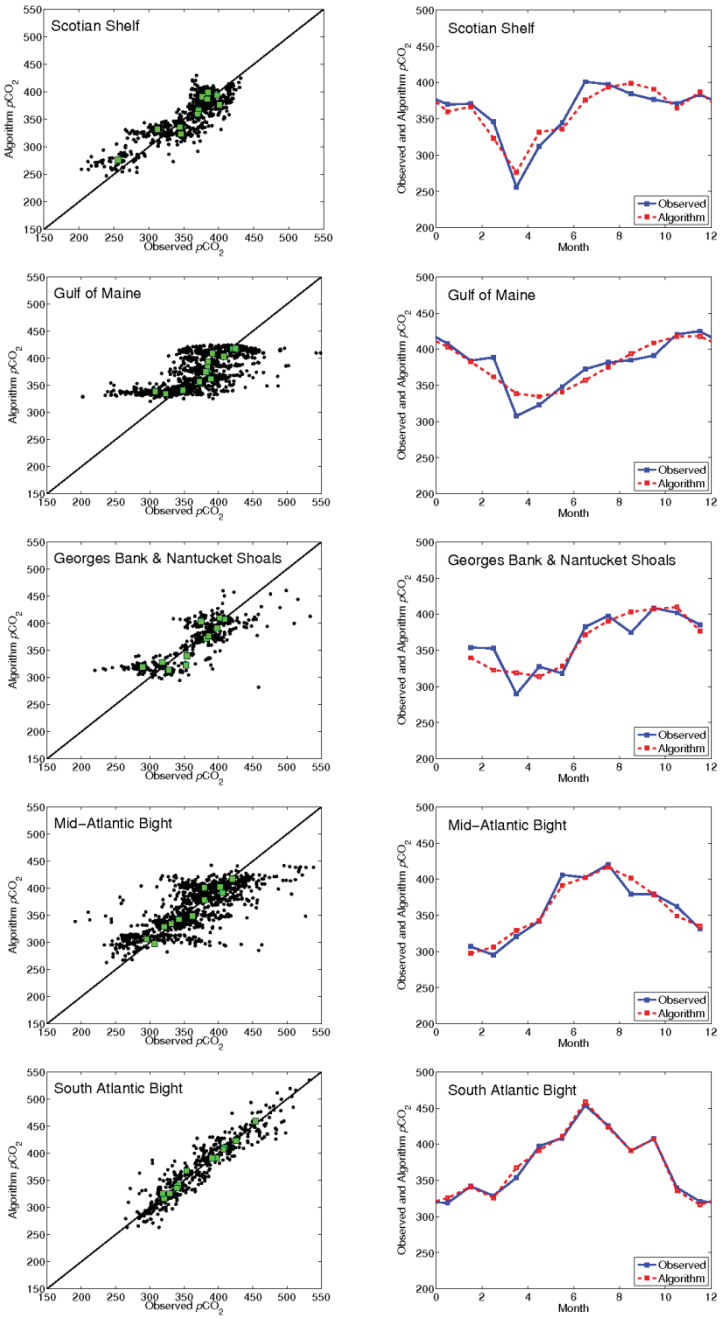

Fig. 5. From top to bottom: scatter plots (left column) of observed (SOCAT) vs. algorithm (Equation 1) pCO_2 (μatm) for the five regions (black dots all months, green squares monthly ensemble averages). The right column shows the mean seasonal plots of the ensemble averages for the equivalent regions. There are no data available for the MAB and GB+NS for January. Only data bins with more than six months of coverage were used.

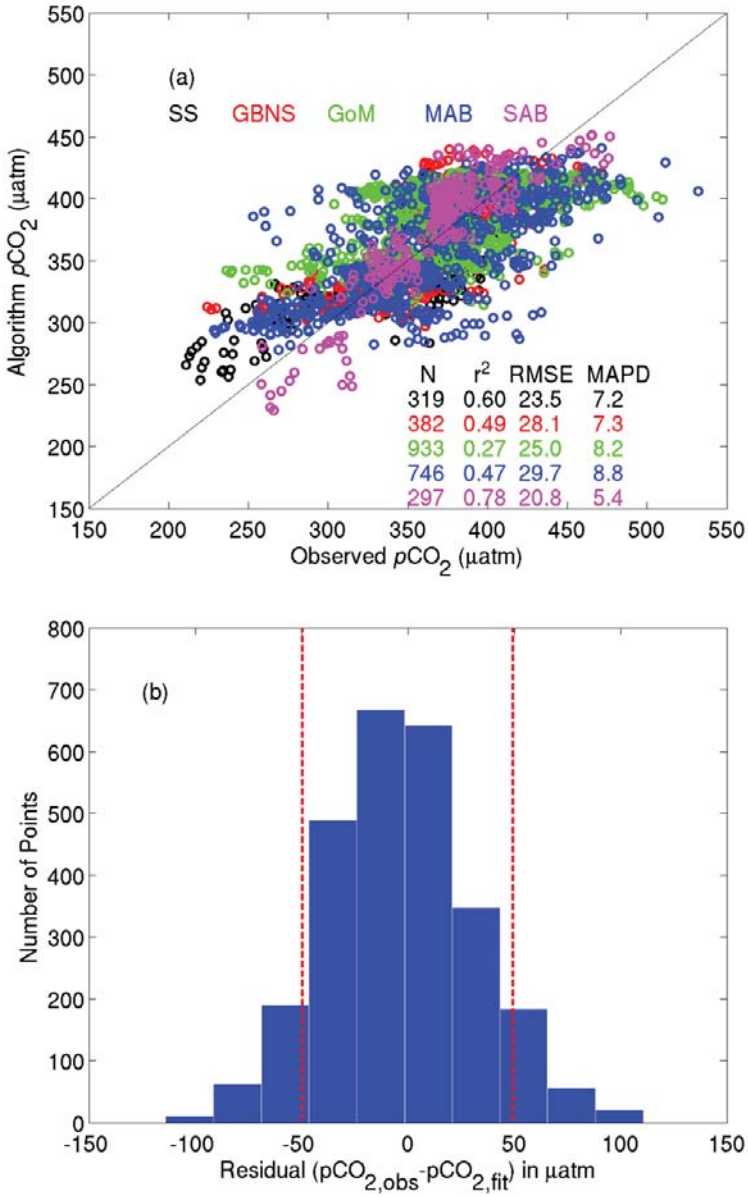

Fig. 6. (a) Scatter plot of algorithm versus observed surface ocean pCO_2 based on observed values not used in the algorithm development (bins with temporal coverage less than 6 months). The r^2, RMSE, and mean absolute percent difference (MAPD) are shown in the legend. (b) Histogram of residuals (observed minus algorithm). The red dashed vertical lines represent the standard deviation ($\pm\sigma$) of the observed pCO_2.

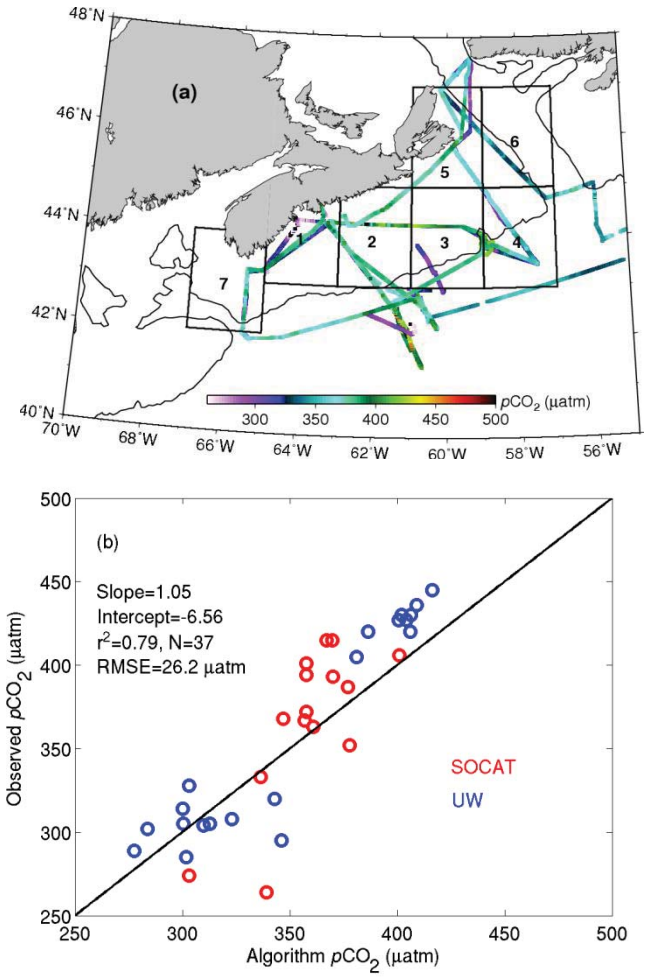

Fig. 7. (a) Map showing the seven 2^{o}x2^{o} boxes covering the entire Scotian Shelf (SS) region adapted from *Shadwick et al*. [2010]. The contour line is the 200 m isobath. The algorithm and *in situ* (SOCAT (not shown) and UW observations from Dalhousie University cruises) mean surface ocean pCO_2 were obtained for each of the seven boxes for evaluation purposes. The scatter plot of algorithm versus observed pCO_2 for all seven boxes is shown in (b) with corresponding statistics in the legend.

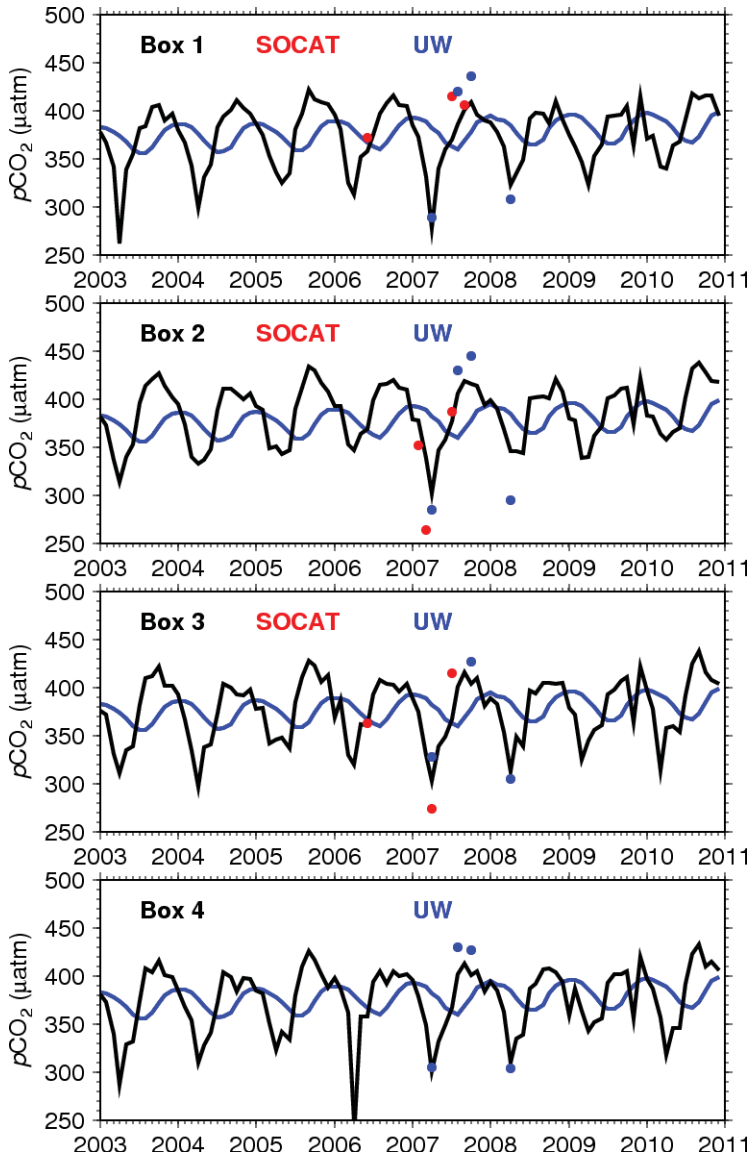

Fig. 8a. Time series of algorithm mean surface ocean pCO_2 (black lines) for boxes 1 through 4 shown in Fig. 7a. The corresponding SOCAT (red dots) and Dalhousie UW (blue dots) data are shown for comparison. The blue lines are the atmospheric pCO_2. See Fig. 7b for statistical evaluation.

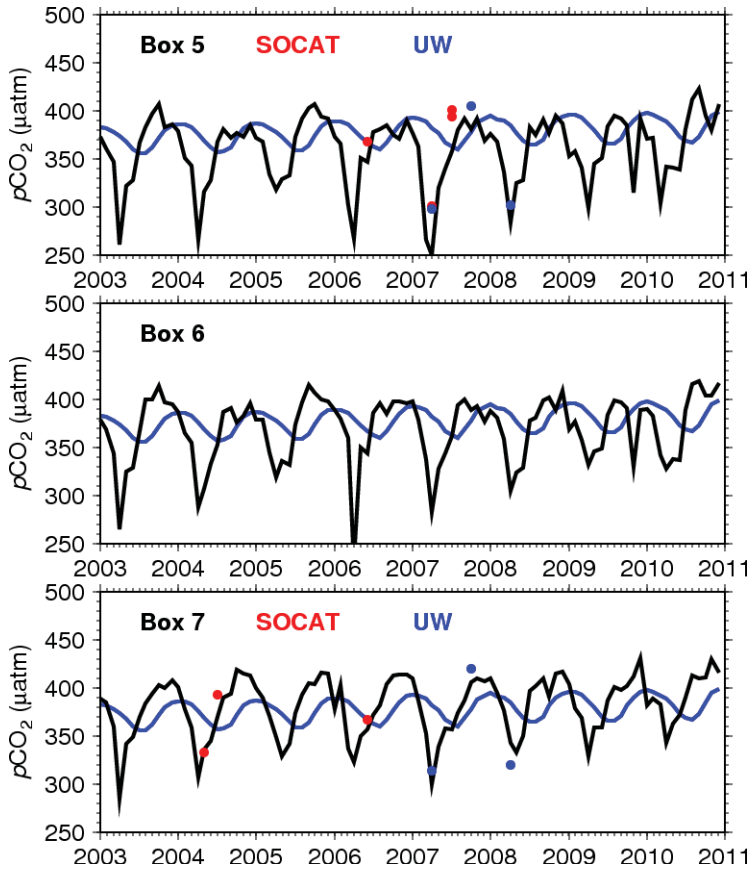

Fig. 8b. Time series of algorithm mean surface ocean pCO_2 (black lines) for boxes 5, 6 and 7 shown in Fig. 7a. The corresponding SOCAT (red dots) and Dalhousie UW (blue dots) data are shown for comparison. The blue lines are the atmospheric pCO_2. See Fig. 7b for statistical evaluation.

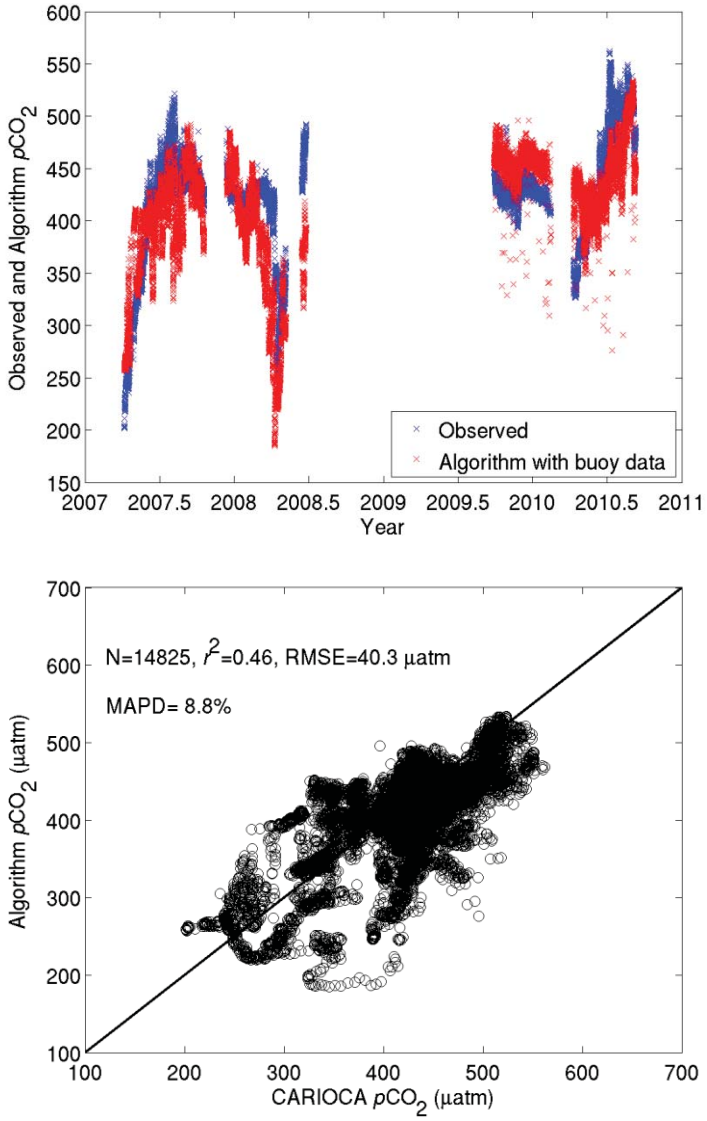

Fig. 9. Time series of high frequency (hourly) surface ocean pCO_2 measured (blue crosses) at the Carioca buoy from 2007 to 2010, and corresponding algorithm prediction (red crosses) using hourly values of SST, SSS, and calibrated fluorometer Chl as inputs (top panel). The scatter plot of observed vs. algorithm pCO_2 is shown in the bottom panel.

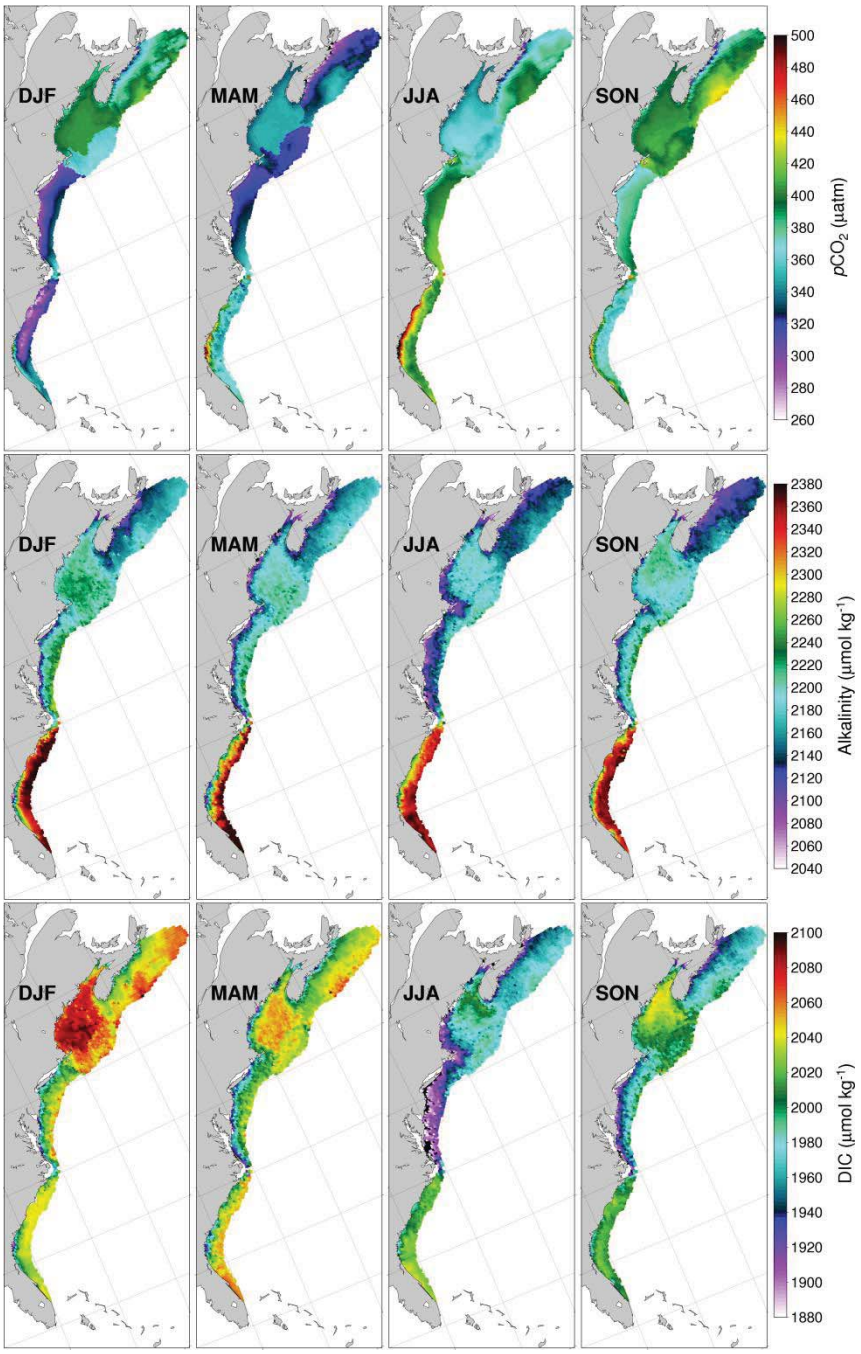

Fig. 10. Seasonal maps of algorithm pCO_2, salinity-derived alkalinity from *Cai et al.* [2010] equations, and DIC derived from alkalinity and algorithm pCO_2. The seasons are defined as Dec-Jan-Feb (DJF), Mar-Apr-May (MAM), Jun-Jul-Aug (JJA), and Sep-Oct-Nov (SON).

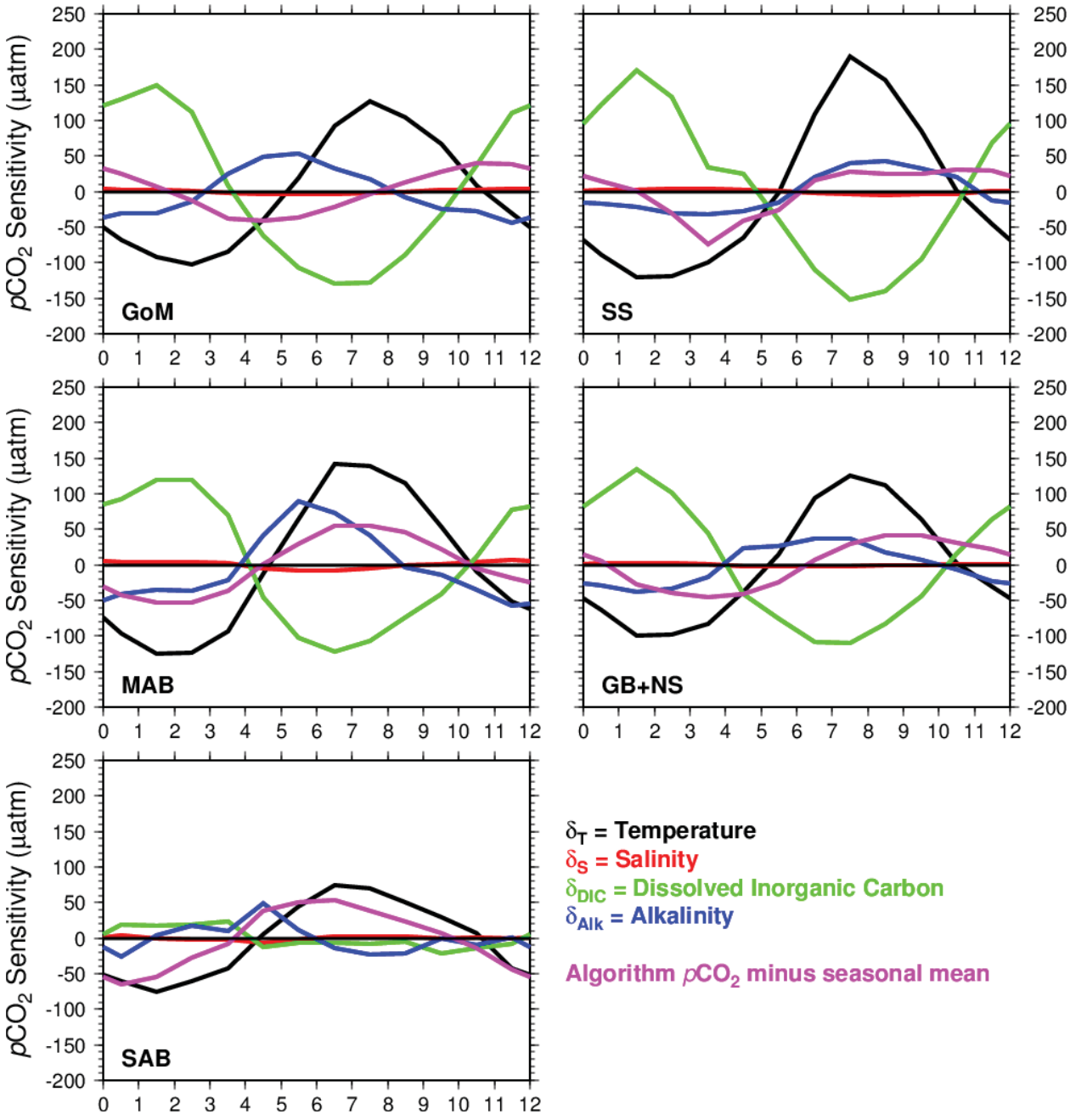

Fig. 11. Sensitivity of pCO_2 seasonal cycle to most influential parameters. Alkalinity was derived using SSS from monthly WOA 2009 salinity data (*D. Tomaso* personal communication, 2012), spatially interpolated using Kriging, and *Cai et al.* [2010] equations. DIC was derived from algorithm pCO_2, alkalinity, WOA SSS, and MODIS SST. Refer to text for methodology to derive parameter sensitivity.

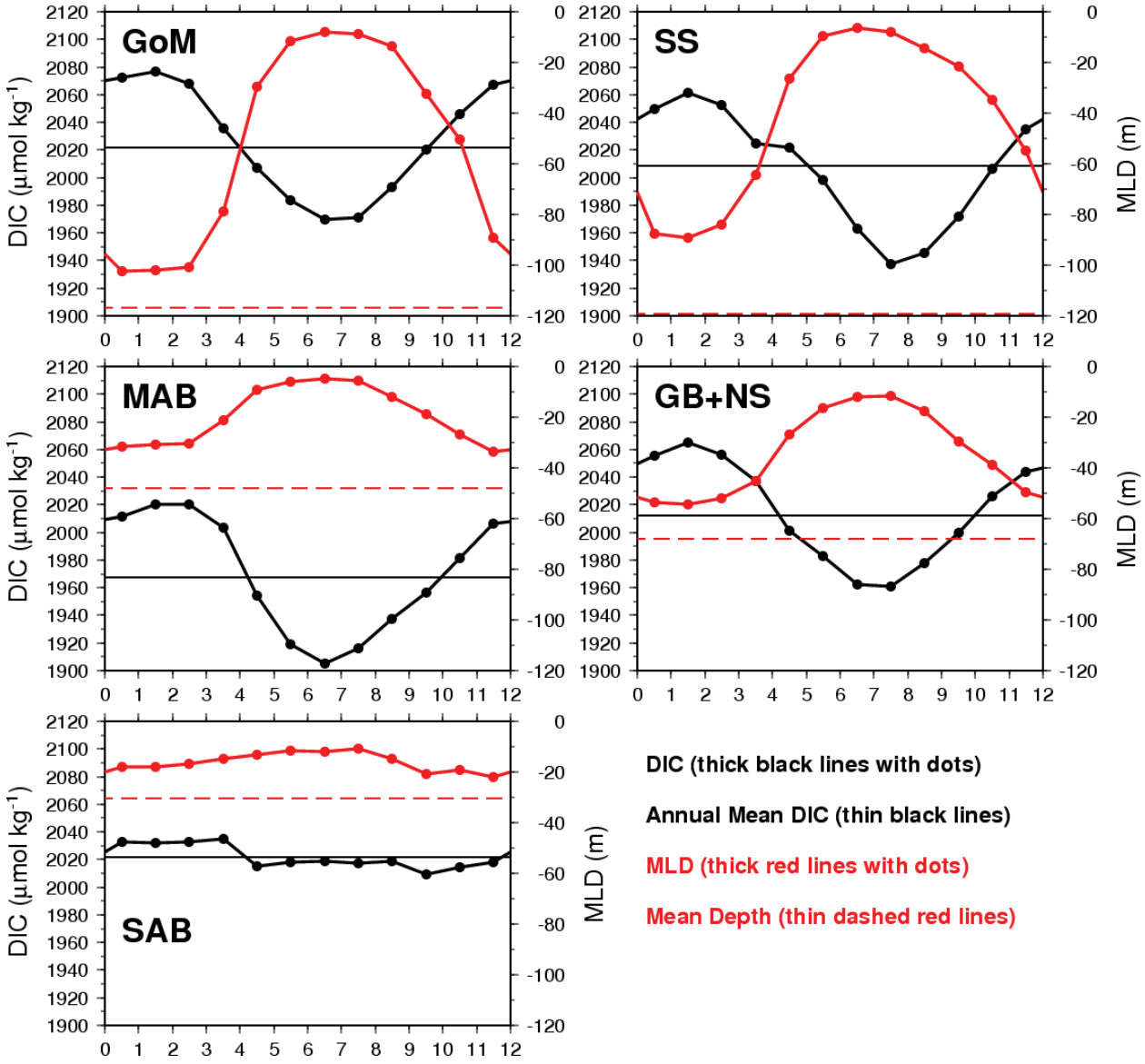

Fig. 12. Regionally averaged seasonal DIC (black lines and circles) derived from TA (SSS) [Cai et al., 2010], SST from MODIS, monthly SSS from WOA 2009 (*D. Tomaso* personal communication, 2012) spatially interpolated using Kriging, and algorithm pCO_2. The seasonal mixed layer depth (MLD) is superposed for each region (red lines and circles). The red dashed lines represent the mean bottom depth for each region and the thin black lines are the annual mean DIC for each region, with the GoM and SAB having the highest values (2022 µmol kg^{-1}) and the MAB the lowest (1968 µmol kg^{-1}).

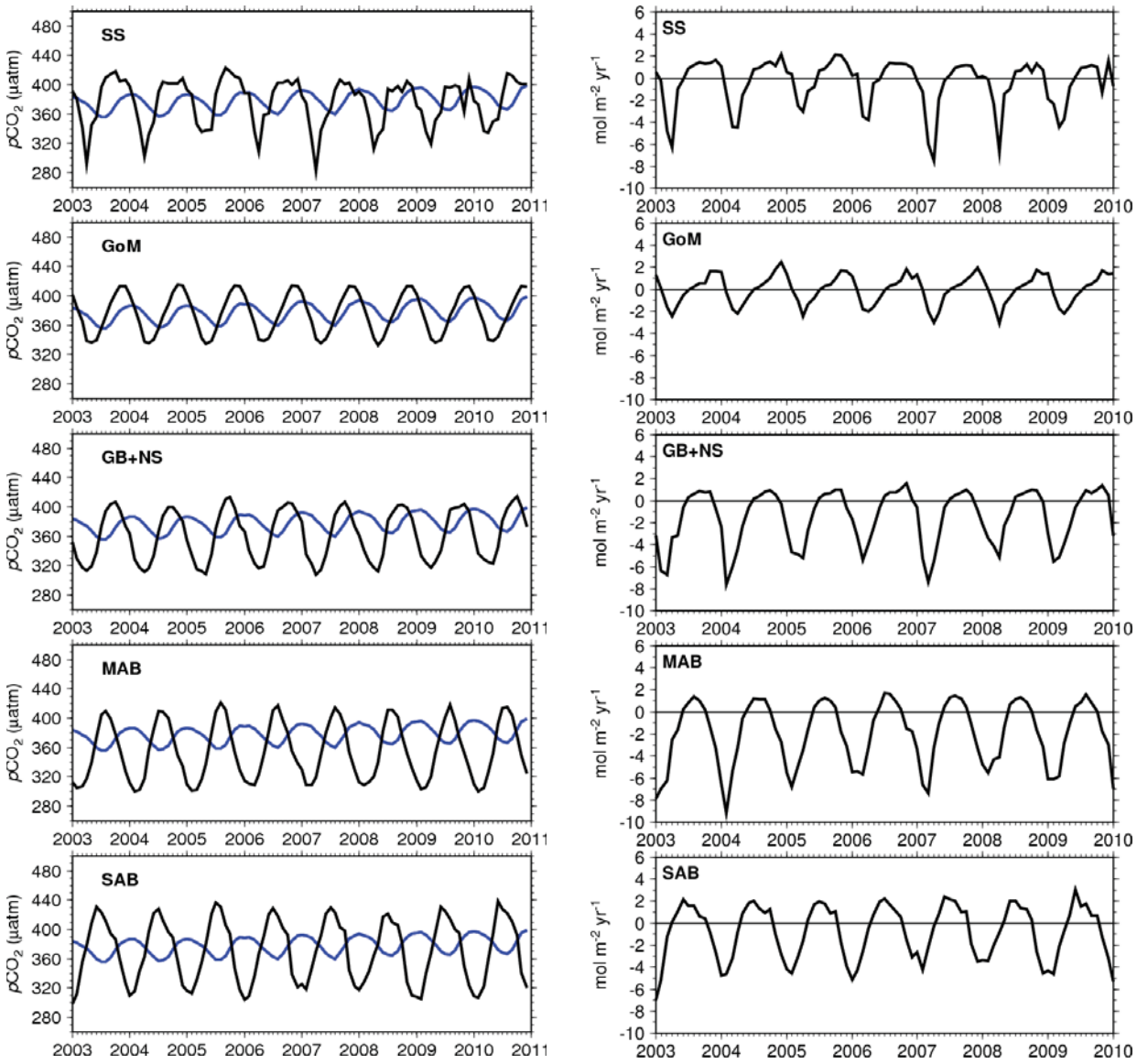

Fig. 13. Left panel: Monthly surface ocean pCO_2 derived from algorithm (black lines) and atmospheric pCO_2 from Grifton, NC located at 35.53°N and 77.38°W (superposed blue lines). Right panel: Sea-air CO_2 flux derived from ΔpCO_2, CCMP winds, and *Ho et al.* [2011] gas transfer parameterization.

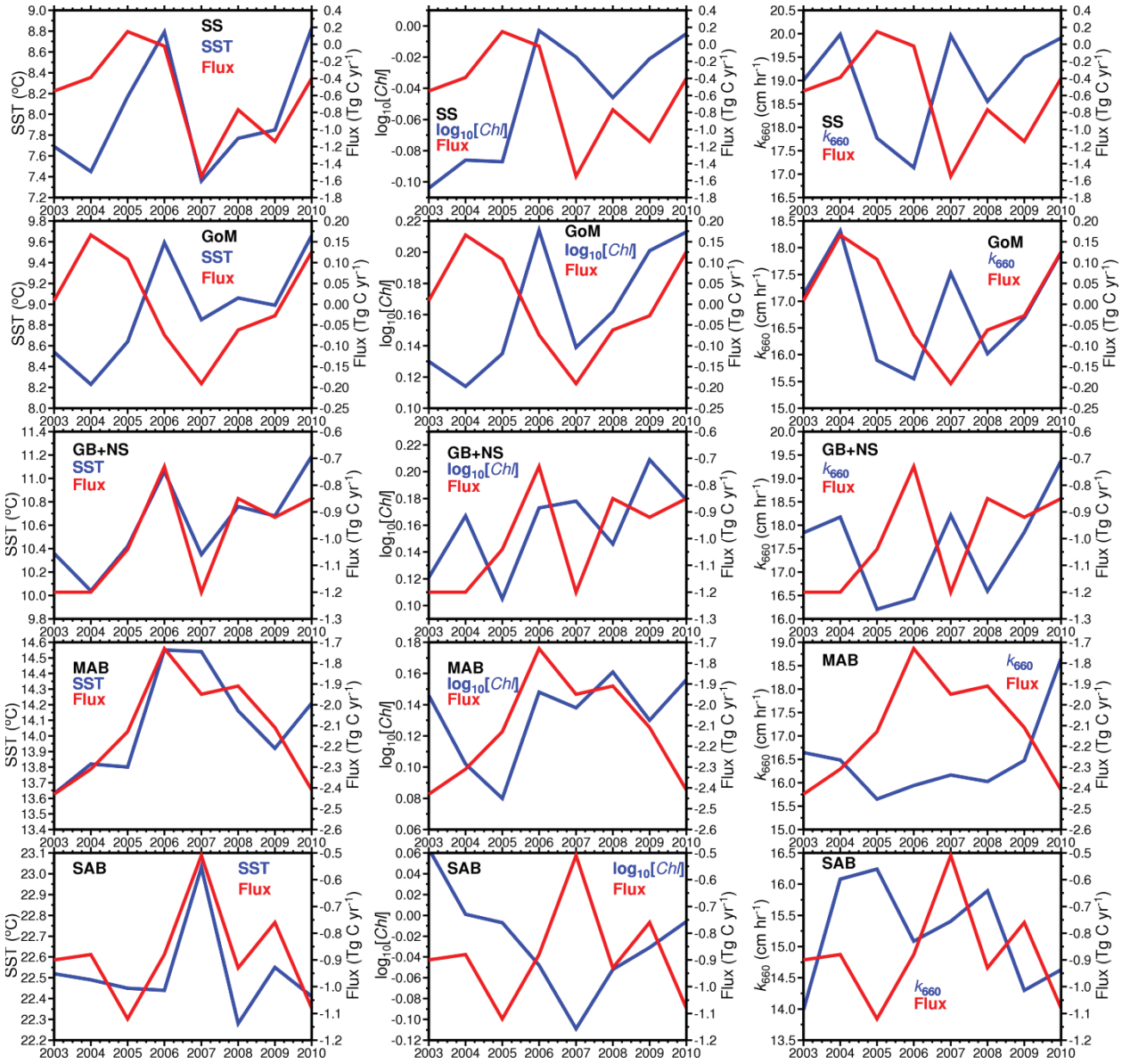

Fig. 14. Mean annual sea-air CO_2 flux (red lines, Tg C yr^{-1}) combined with SST (^{o}C), log10[*Chl*] (blue lines) and k_{660} (cm hr^{-1}, blue lines) for all 5 regions

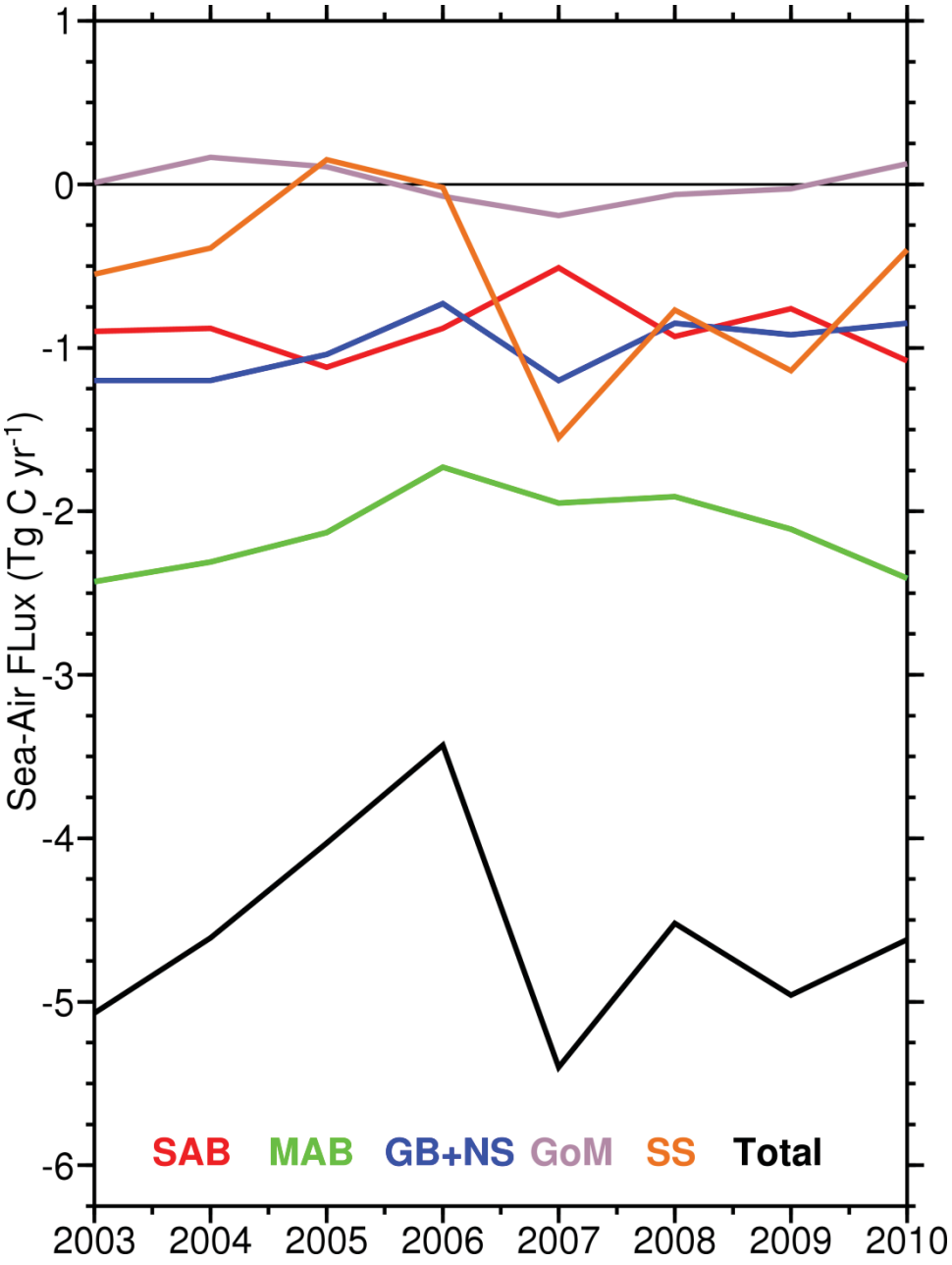

Fig.15. Time series of algorithm annual sea-air CO_2 flux for all five individual regions and for the entire east coast.

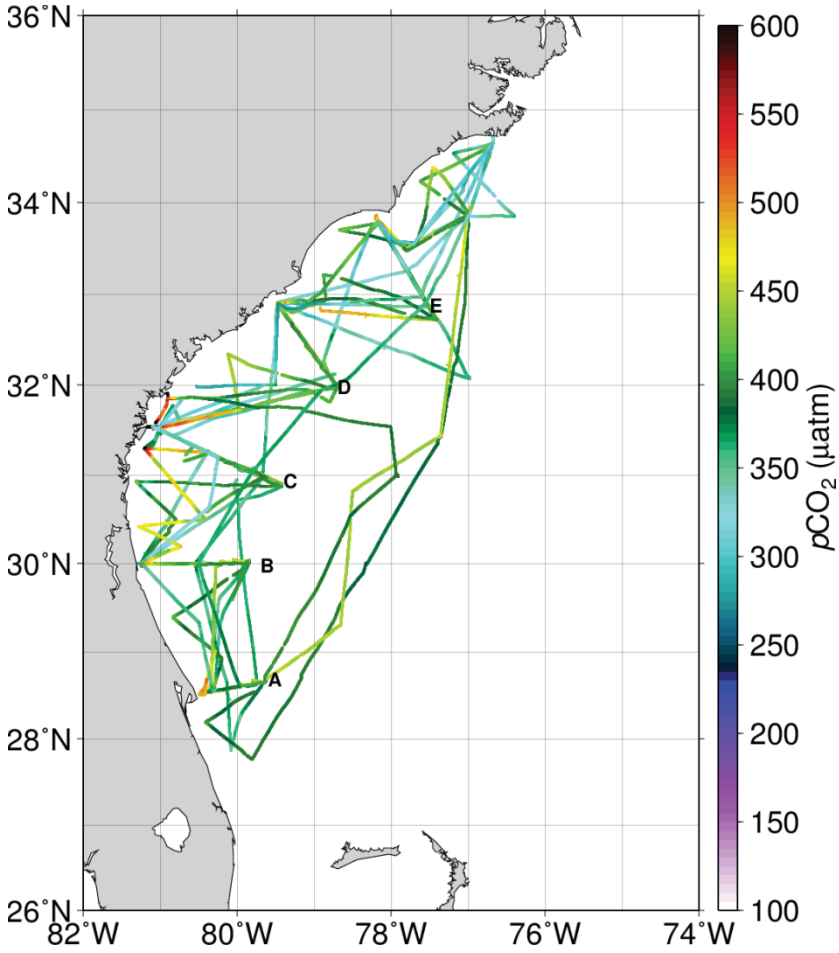

Fig. A-1. Distribution of underway pCO_2 tracks in the SAB.

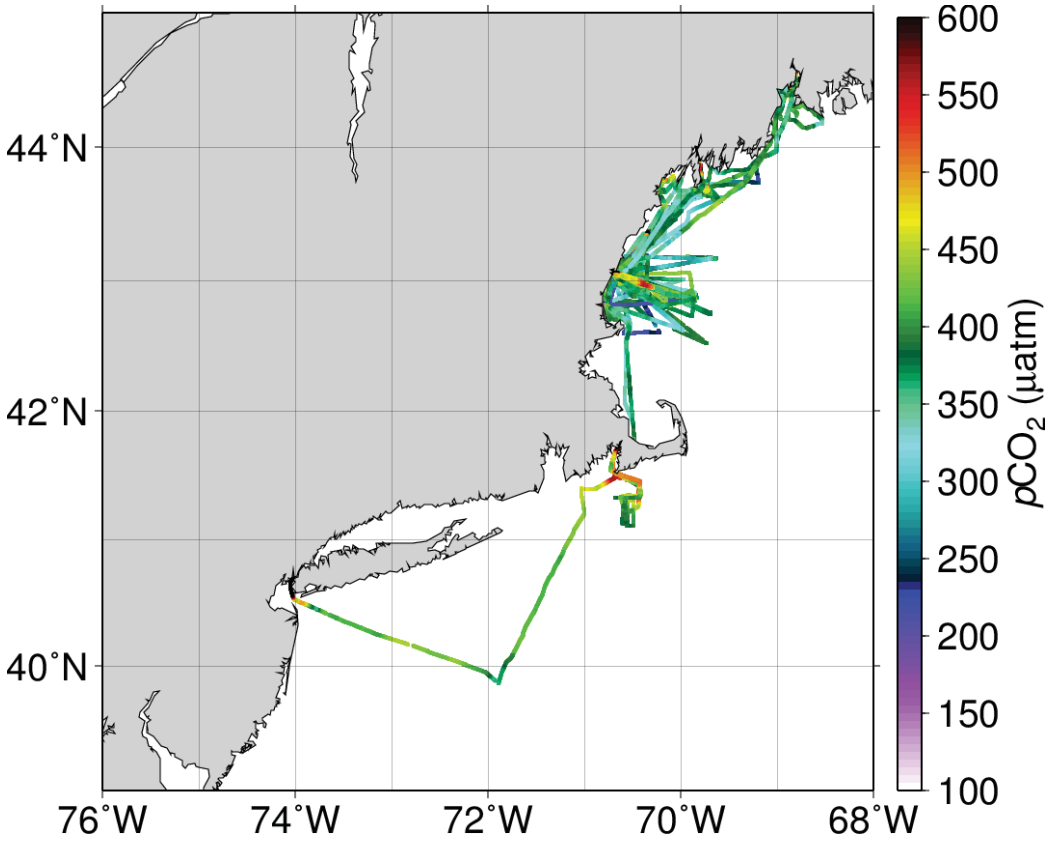

Fig. A-2. Map showing the underway pCO_2 tracks in the GoM and a single cruise track from Woods Hole to New York City.